Werner Kleinsasser, BSc.

Molecular beam setup to investigate ultrafast dynamics in isolated molecular clusters

Master's Thesis

to achieve the university degree of

Diplom-Ingenieur

Master's degrees programme: Technichal Physics

submitted to

Graz University of Technology

Supervisor

Assoc.-Prof. Dipl.Ing. Dr. Markus Koch

Institute of Experimental Physics

Graz, June 2019

Affidavit

I declare that I have authored this thesis independently, that I have not used other than the declared sources/resources and that I have explicitly indicated all material which has been quoted either literally or by content from the sources used. The text document uploaded to TUGRAZonline is identical to the present master thesis.

_____   _____

city, date   *signature*

Eidesstadtliche Erklärung

Ich erkläre an Eides statt, dass ich die vorliegende Arbeit selbstständig verfasst, andere als die angegebenen Quellen/Hilfsmittel nicht benutzt und die den benutzten Quellen wörtlich und inhaltlich entnommenen Stellen als solche kenntlich gemacht habe. Das in TUGRAZonline hochgeladene Textdokument ist mit der vorliegenden Diplomarbeit identisch.

_____   _____

Ort, Datum   *Unterschrift*

Abstract

In analogy to an exisiting system from Femtolab I, a new setup for investigating the photocatalytic water splitting process via femtosecond pump-probe laser spectroscopy was designed and built. The nozzle situated in the source chamber of a UHV system creates a molecular seeded beam through free jet expansion. To avoid clogging of the nozzle, a three-stage controller circuit for heating was designed. Either a time-of-flight (TOF) spectrometer for electrons and ions in magnetic bottle configuration and MCP detector, or a quadrupole mass spectrometer (QMS) are used for detection and analyzing. The TOF was improved by implementing a third plate, leading to a two-stage-acceleration Wiley McLaren setup for better spatial focusing. The ionized system can be measured with photoelectron photoion coincidence (PEPICO). After building the setup, the whole system was checked for leaks and first molecular beam measurements were done with pressure and temperature dependencies of the nozzle. Characterization measurements of the TOF were made by varying the voltages at the MCP and the repeller, as well as the solenoid current, followed by varying the magnet positions with a manipulator. With this setup, a new field of research is established and will be investigated over the following years. The photocatalytic water splitting process can be examined on chromophore-water-clusters that have been studied in simulations over the past years. This is a promising approach to create hydrogen that can be used as a renewable energy source. Additionaly, the CO_2 pollution can be reduced by converting the CO_2 to valuable sources like ethanol.

Kurzfassung

Basierend auf einem bestehenden System aus dem Femtolab I wurde eine neue Apparatur entworfen und gebaut, um die photokatalytische Wasserspaltung mittels femtosekunden pump-probe Laserspektroskopie zu untersuchen. In einem Ultrahochvakuum befindet sich die Düse in der Quellkammer, die über Freistrahlexpansion einen Molekülstrahl erzeugt. Um eine Verstopfung der Düse zu vermeiden, wurde eine dreistufige Steuerschaltung für die Heizung entworfen und gebaut. Als Analysatoren und Detektoren dienen entweder ein Flugzeitspektrometer (TOF) für Elektronen und Ionen mit magnetic bottle Konfiguration und MCP, oder ein QMS. Das TOF wurde für eine bessere Ortsfokussierung durch eine dritte Platte zu einem zwei-Stufen-Beschleunigung Wiley McLaren Setup verbessert. Das ionisierte System kann mit Photoelektron-Photoion-Koinzidenz gemessen werden. Nach dem Aufbau wurde das System auf Lecks untersucht und erste Molekülstrahlmessungen wurden mit Druck- und Temperaturverhalten der Düse durchgeführt. Das TOF wurde durch Variation der MCP- und Repellerspannungen, sowie des Spulenstroms und der Positionen des Magneten mit einem Manipulator charakterisiert. Dieser Aufbau führt zu einem neuen Forschungsgebiet, das in den nächsten Jahren untersucht wird. Zukünftig werden Chromophor-Wasser-Cluster untersucht, die in den letzten Jahren in Simulationen berechnet wurden. Dies ist eine vielversprechende Methode, um Wasserstoff zu generieren, der als erneuerbare Energiequelle dient. Zusätzlich kann auch die CO_2-Verschmutzung reduziert werden, indem CO_2 zu anderen Energiequellen wie Ethanol umgeformt wird.

Table of Contents

CHAPTER 1

Introduction

Photocatalysis is a new research branch and a sophisticated way to produce hydrogen using light, water and a catalyst. If used in a solvent like water it leads to the so called photocatalytic water splitting process. In the past couple of years there has been much research [1] and there have been many simulations [3–12], but no technology has been commercialized so far.

The ultrafast laser spectroscopy group of M. Koch at TU Graz in cooperation with M. Kitzler at the photonics institute of TU Vienna started the photocatalytic water splitting project with an experimental program for several years. To obtain more information about the molecules used and their behaviour, the group of Markus Koch at the TU Graz will investigate electron structure dynamics using time resolved photo electron photo ion coincidence (described in section 3.1.1), whereas the group of Markus Kitzler at the TU Vienna will examine nuclear structure changes using time resolved coulomb explosion imaging (described in section 2.3.4).

This section shall provide the reader with the basic knowledge about renewable energy sources and the idea of hydrogen production. Section 2 gives an overview about

the photocatalytic water splitting process and the questions arising that will be investigated. In section 3 the experimental setup is explained, followed by the results in section 4.

1.1   On the way to renewable energy sources

There are several approaches to utilize alternative energy sources. Photovoltaic cells use the incident sunlight to create charge separation (i.e. voltage) through the photovoltaic effect. A disadvantage is to store the energy efficiently and the dependency on the sun. The efficiency for commercial cells is around 15%. Windpower has a similar problem: if there is too much wind or no wind at all, the power can't be used. And there is also the problem with energy storage. The efficiency for wind power is around 40%.

Another promising approach is to use gaseous hydrogen. Hydrogen is the most common element in the universe and available in many different molecules. Water (H_2O) for example consists of two hydrogen atoms and one oxygen atom and is nearly inexhaustible on Earth. One advantage of gaseous hydrogen and a common misconception is that it can be stored nearly without any losses. Also, it is a so called 'clean' energy source, which means that ideally no pollution takes place at all. If used as a fuel, hydrogen reacts to water again. Because only a transformation from water to hydrogen and back, it is a renewable energy source. Hydrogen can also be used as a fuel in the liquid state. However, the cooling to remain in this state demands quite an energy which reduces the efficiency. So, the remaining problem is to 'create' hydrogen (i.e. dissociate from a molecule) efficiently.

1.2 Hydrogen generation

Hydrogen can be created via electrolysis (fig. 1.1(a)), using water for example - therefore it is also called water-splitting. If a voltage is applied between anode and cathode, water can react at the anode and splits up into oxygen and positively charged hydrogen, thus protons. The protons can diffuse through a membrane and recombine with an electron at the cathode, which neutralizes the positively charged hydrogen atom again. In this way, water and electrical energy produce H_2 and O_2. The reaction formula reads:

$$H_2O \rightarrow \frac{1}{2}O_2 + 2H^+ + 2e^-$$
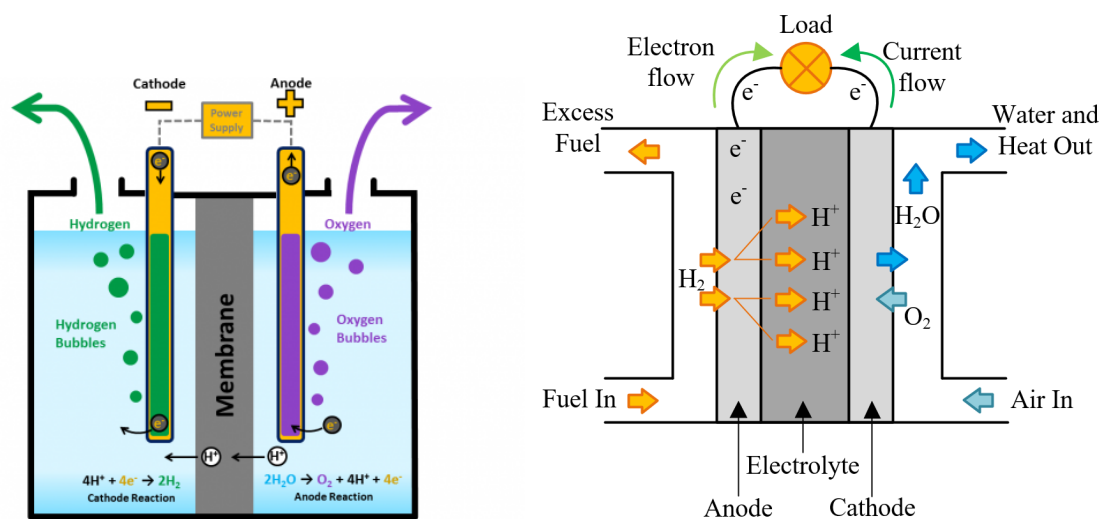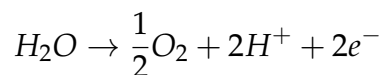
(a) Electrolysis, source: [30]

(b) Fuel cell, source: [31]

Figure 1.1: Principle of hydrogen creation via electrolysis and the usage of hydrogen as energy source. Explained in detail in the text.

To get an idea how to use hydrogen as energy source, fig. 1.1(b) shows the schematic atomic, molecular and electronic flow within a fuel cell, which is the inverted process of electrolysis. Here, we see a proton electrolyte membrane (PEM) cell. There are

other versions of fuel cells, but the principle is the same. On the left side at the anode the fuel (H_2) enters and is split at the anode, leading to protons diffusing through the electrolyte. At the cathode, air (O_2)[1] gets in and reacts at the cathode with the protons, leading to double positively loaded H_2O molecules. Because the electrons have to take a detour over a load, the water molecules are neutralized and the current can be used as energy source. The reaction formula is therefore:

$$2H_2 + O_2 \rightarrow H_2O + 2e^-$$
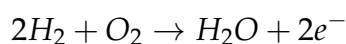
Because only water and heat are created, this should emphasize how eco-friendly and renewable this process is. The efficiency of fuel cells is about 40-60% which can be increased to 85% if the produced heat is also used.

1.3   Photolysis

A rather new approach is to replace the eletrical energy source from the electrolysis with photons for water-splitting, thus the name photolysis. The reaction formula should be:

$$H_2O + h\nu \rightarrow H^\bullet + OH^\bullet$$
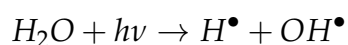
where the dots symbolize radicals[2].

Ideally (and possible for future experiments) sunlight can be used to dissociate hydrogen from water. However, the photon energy of the solar spectrum is far lower than the binding energy of the water molecule, as seen in figure 1.2. For one H_2O molecule, an energy of about 5 eV would be needed and the solar spectrum is beneath $4\,eV$. Therefore, a catalyst is needed, which leads to photocatalysis.

One possibility is to use semiconductors in water (fig. 1.3) [5, 9, 11, 12]. If the incident light is in the regime of the band gap, electrons and holes are created. Water

---

[1] Actually, the term 'air' involves about 80% N_2 and only about 20% O_2

[2] A radical is an atom or a molecule with an unpaired valence electron and therefore highly reactive.
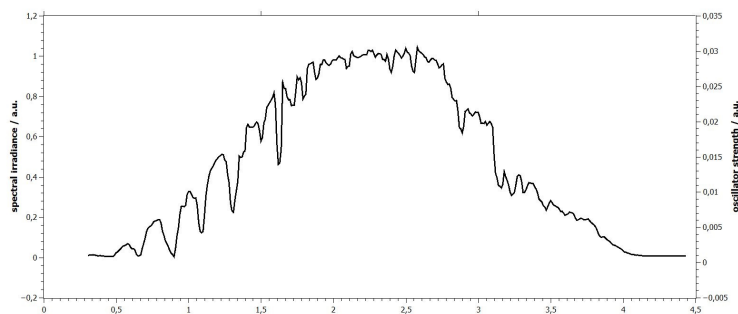
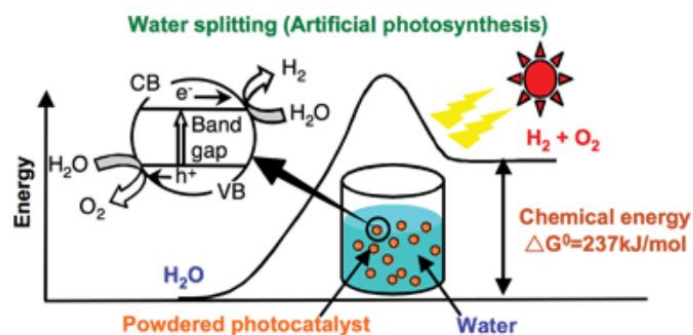**Figure 1.2:** Solar spectrum at the surface of the earth. Source: [5, 9, 11, 12]

Figure 1.3: Principle of hydrogen production via semiconductor. Source: [2]

can then be split into H_2 and O_2. Experiments have shown, that due to the fast electron-holes recombination, the efficiency of this process is only about 19% [**?**]. Therefore, a more efficient approach was proposed and will be discussed in section 2.

CHAPTER 2

# Photocatalysis

As mentioned in section 1.3, hydrogen can be obtained through water splitting. Prof. W. Domcke of the TU Munich has performed many quantum chemical simulations over the past years [3] and suggested a water-splitting cycle described in the following section. The first goal will be to test these calculations with actual measurements.

2.1 Photocatalytic water splitting

Fig.2.1 shows the schematic cycle of photocatalytic water splitting. The molecule at (1) is called Pyridine (PY) which is basically a benzene molecule where one C atom with its H atom is replaced by one N atom. The other molecules used in this project are described later (sec. 2.2).
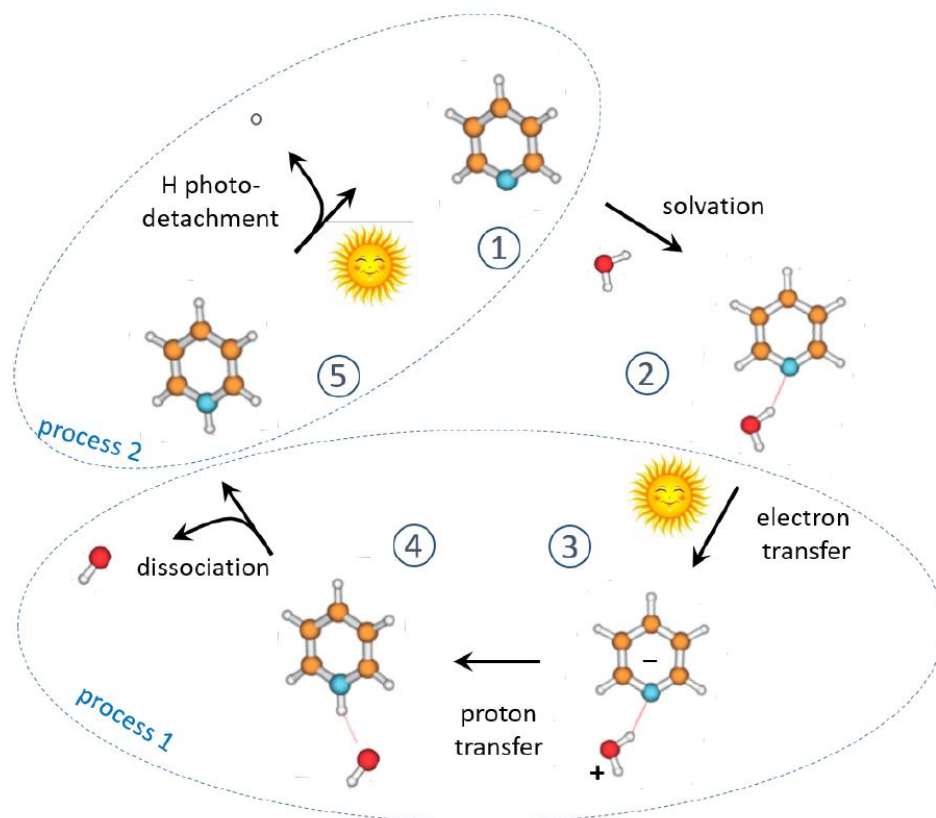
Figure 2.1: Overview of the photoinduced water splitting cycle. Explained in detail in the text. Adapted from [5]

If the PY molecule (1) is solvated in water (2), hydrogen bonds between the hydrogen and the nitrogen atoms are formed. After absorption of a photon symbolized by the sun (3), an electron transfer from water to the PY takes place. This is responsible for a subsequent proton transfer (4), leaving a pyridinium radical (PYH$^\bullet$) and a hydroxyl radical (OH$^\bullet$). Because these two processes are coupled, we speak of an electron-driven-proton-transfer (EDPT). Ideally, this EDPT provides the system with the energy to dissociate the hydroxyl. If a second photon is absorbed by the PYH$^\bullet$ in (5), the H can be detached, leaving a PY molecule and closing the cycle.

Two main processes can be identified through the water-splitting-cycle: the EDPT and the H-detachment, which will be described in detail in section 2.3. The EDPT is ex-
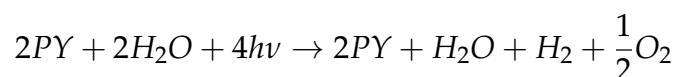
perimentally not well understood, but there are many calculations, especially for PY [5].

This cycle leads to the reaction formula

$$PY + H_2O + 2h\nu \rightarrow PY + H^\bullet + OH^\bullet$$
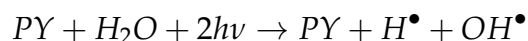
or, multiplied by 2 and taken the fact that the radicals can react in dark reactions (i.e. where no light is needed):

$$2PY + 2H_2O + 4h\nu \rightarrow 2PY + H_2O + H_2 + \frac{1}{2}O_2$$
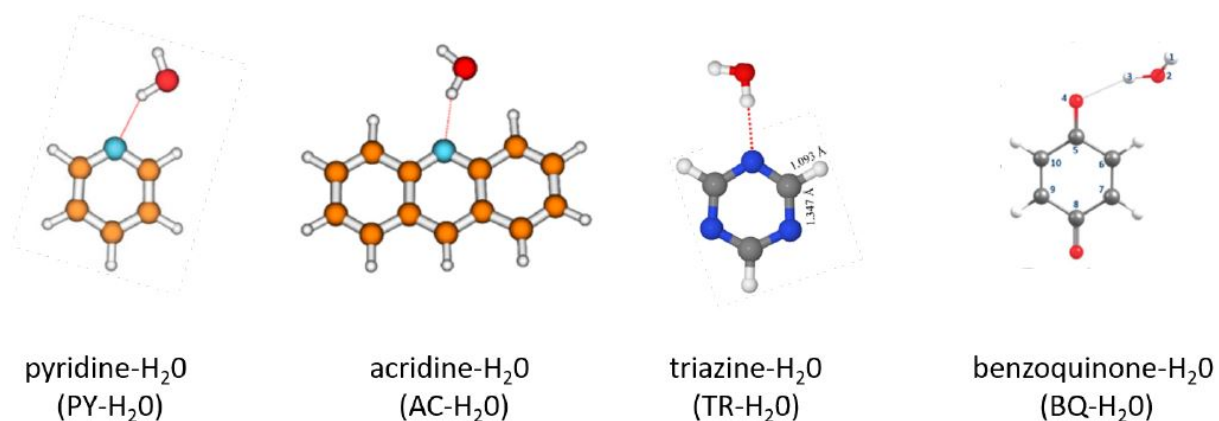
Qualitatively, about 50% of the photon energies are converted into chemical energy of the radicals [12]. Compared with the efficiency of the semiconductor-approach (sec.1.3) with 10%, this seems rather promising.

2.2 Chromophores

The chemicals used are called chromophores. Those investigated are shown in figure 2.2. Although, they might not be the answer for sunlight-water-splitting, there have been many studies about those molecules [5–8], which will be compared by future measurements. The predictions of the reaction dynamics are similar for all the chromophores used.
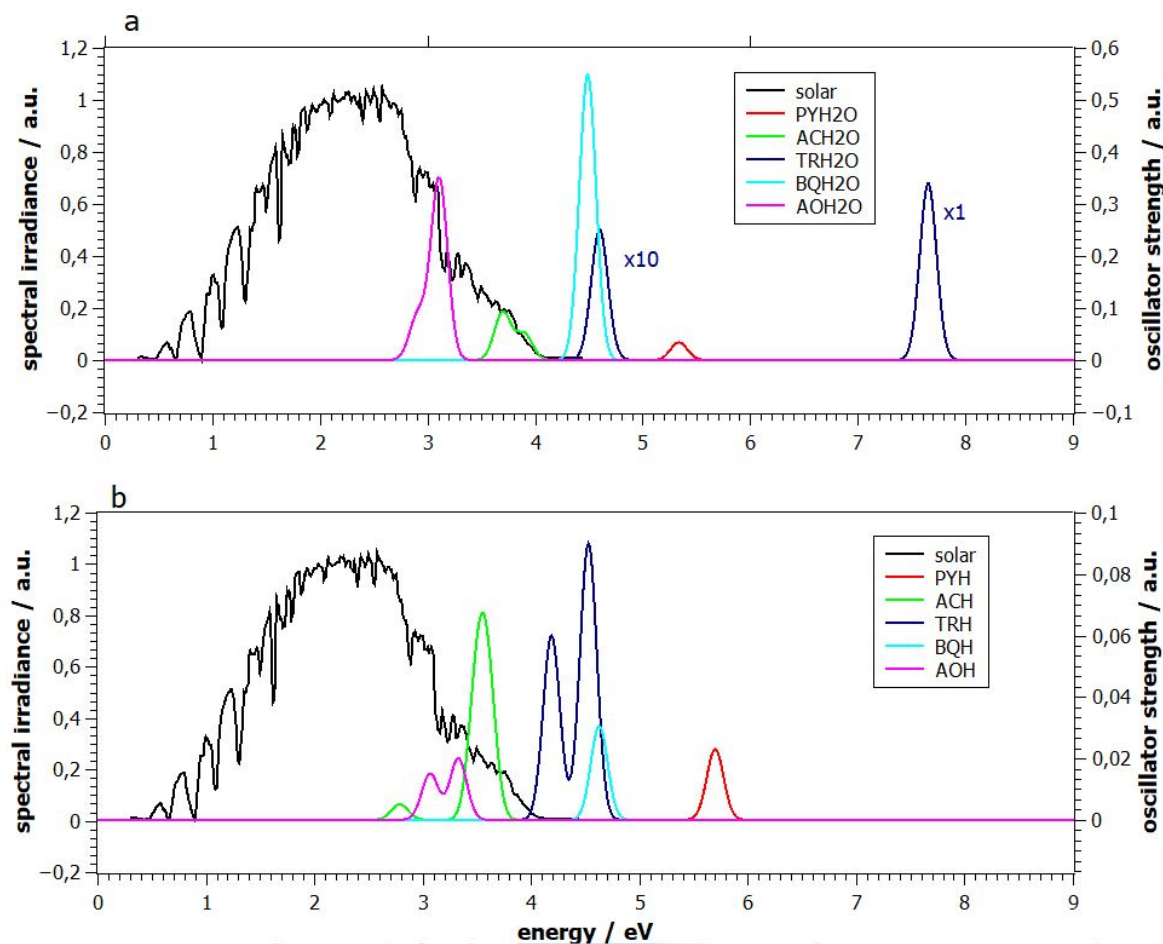
In figure 2.3 the absorption spectra of the chromophores can be seen as a function of energy in eV. The top figure shows the chromophore-H_2O absorption, respectively the EDPT-process and the lower shows the chromophore-H radicals, respectively the H-detachment-process. The solar spectrum is also included (black lines). Those spectra are only calculated and have to be investigated experimentally. Additional information about the chemical properties is found in [38, 39].

pyridine-H$_2$0
(PY-H$_2$0)

acridine-H$_2$0
(AC-H$_2$0)

triazine-H$_2$0
(TR-H$_2$0)

benzoquinone-H$_2$0
(BQ-H$_2$0)

Figure 2.2: Different catalyst molecules used with a bound water-molecule

Table 2.1: Data of the used chromophores with ionization energies (IE), needed wavelengths for EDPT (λ_{EDPT}), H-detachment (λ_{Hdiss}) and vapor temperature (T_{vap})

chromophore	IE eV	λ_{EDPT} nm (eV)	λ_{Hdiss} nm (eV)	T_{vap} °C
pyridine (PY, C$_5$H$_5$N)	9.3	250 (5.0)	220 (5.7)	25
acridine (AC, C$_{13}$H$_9$N)	7.8	335 (3.7)	390 (3.2)	120
(1,3,5)triazine (TR, C$_3$N$_3$H$_3$)	10.0	2x 310 (2x 4.0)	-	25
(1,4) benzoquinone (BQ, C$_6$H$_4$O$_2$)	10.0	250 (5.0)	250 (5.0)	44

Figure 2.3: Calculated absorption spectra of the used chromophores and solar spectrum. Adapted from [5,9,11,12]

2.2.1 Pyridine (PY)

The red peaks in figure 2.3 are outside the solar spectrum. Therefore, this molecule isn't suitable for sunlight-water-splitting. However, there are many theoretical calculations, so it will be the model chromophore.

2.2.2   Acridine (AC), Acridine orange (AO)

AC looks similar to PY but with two more benzene rings around it. This shifts the spectrum in the red (green line) - so it lies within the solar spectrum. However, fluorescence experiments have shown that the EDPT doesn't take place in aqueous solutions. This is why this chromophore will be studied to investigate its behavior in water and in ethanol solutions to understand why it doesn't work in water. AO will also be investigated. Its structure is similar to AC but more shifted in the red (purple line). The measurements are expected to be similar to those of AC.

2.2.3   Triazine (TR)

TR is basically a PY molecule but with three N atoms. There are two absorption spectra which both lie outside of the solar spectrum. W. Domcke has confirmed the EDPT and the H-detachment for TR and H-evolution has been demonstrated [26].

2.2.4   Benzoquinone (BQ)

BQ is also similar to PY but with two O atoms instead of H atoms. BQ again lies outside of the spectrum, however, its structure can be modified to shift it inside. The EDPT is expected to happen much faster because there is no energy barrier between the relevant states mentioned afterwards (sec. 2.3).

2.3   Questions to be answered

Emerging from the photocatalytic water-splitting-cycle, some questions arise from the two processes. These will be the focus studying different chromophores and will be explained in the following sections.

2.3.1 Process 1 - EDPT

In figure 2.4 the potential energy surface of the two states of the EDPT process are shown as a function of the atomic distance of O and H, using PY [5, 6, 13, 14]. Left from the dashed line, the system behaves like a PY-H_2O molecule and, if excited, leading to a locally excited (LE) state. Right from the dashed line, the system behaves like a PYH$^\bullet$-OH$^\bullet$. If the right state is populated, the distance of H and O increases, leading to a charge transfer (CT) state. If this system is excited by a photon from ground state S_0, the LE states are populated regarding the Franck-Condon overlap. There is a conical intersection (blue star) of these states. The small barrier between the LE and the CT states (green star) can be overcome with the energy from the incoming photon.
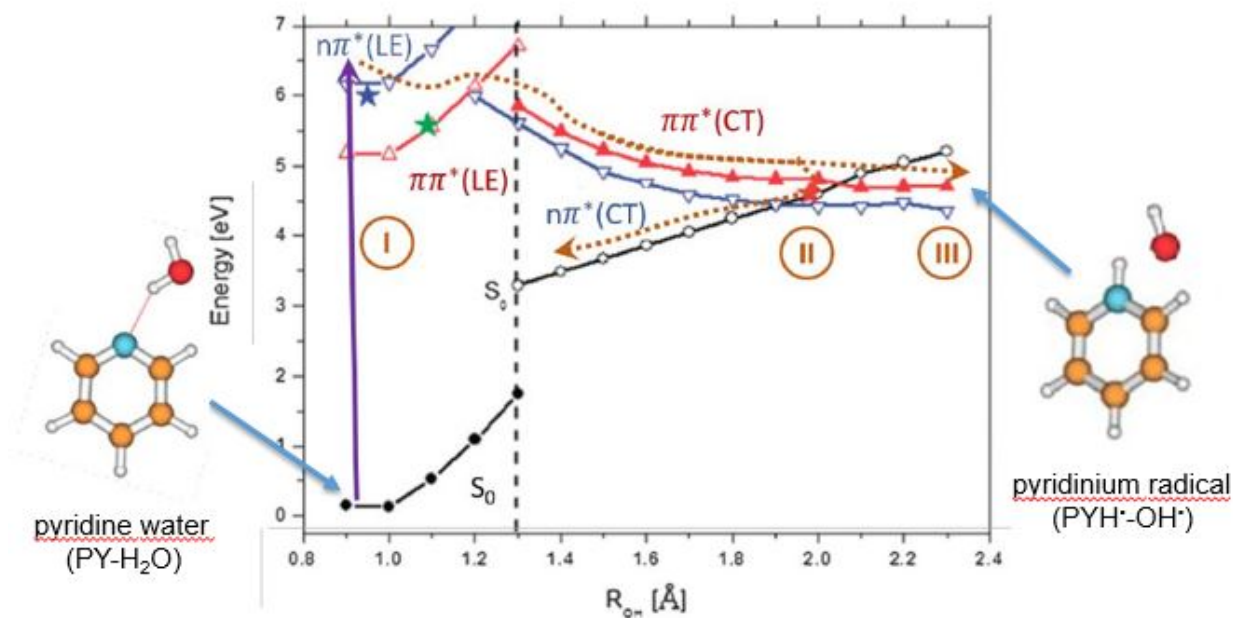
Figure 2.4: Potential energy surface of PY-H_2O and PYH$^\bullet$-OH$^\bullet$. Energy plotted as a function of O-H distance. Source: [5]

From this picture, three questions arise:

1. The exact pathway from LE to CT is not known. There is a barrier, however, also

other paths may be included.

2. Between the ground state and the CT states there is a conical intersection that may lead to intramolecular non-radiative pathways to the ground state, which would prevent the EDPT from happening.

3. Energy can be redistributed to vibrational degrees of freedom that may hinder the dissociation of the hydroxyl radical OH$^{\bullet}$.

Those questions are dependent on the chromophore (e.g. as mentioned before, BQ does not have a barrier between the LE and the CT states and AC has a higher barrier than PY, which leads to a different relaxation behavior).

2.3.2   Process 2 - H-detachment

Figure 2.5 shows the potential energy surface of the states included in the second process - the H-detachment - as a function of the distance of N and H [3, 17–21]. On the left the system behaves like a PYH$^{\bullet}$, whereas on the right the N-H-distance increases and the H is detached and the system leads back to the PY. If the ground state D_0 is excited, the reaction path may look like the brown dashed line.
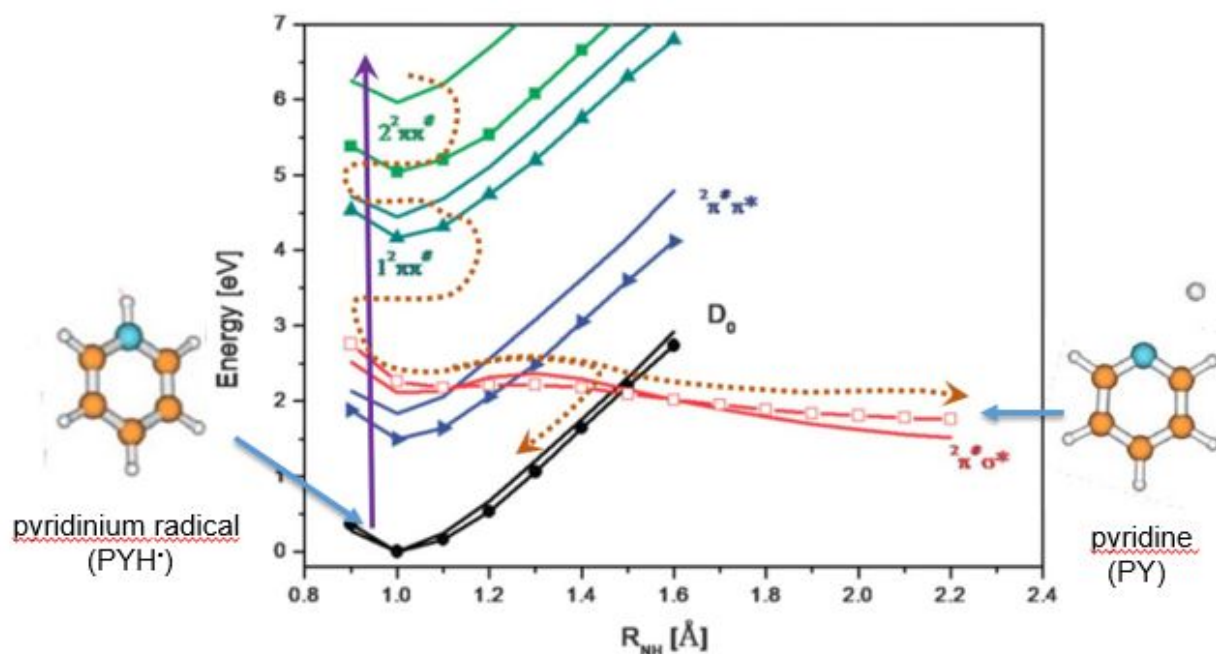
Figure 2.5: Potential energy surface of PYH$^\bullet$ and PY. Energy plotted as a function of N-H distance.

For this process, two more questions arise:

4. The exact pathway from the excited state is not known. There might be crossings that interfere and prevent the H from detaching.

5. Again, there is a conical intersection with the ground state that might lead to a population transfer back to the ground state.

2.3.3 Answers

Figure 2.6 shows a kinetic model based on quantum chemical calculations that will help the interpretation of the experimental concerning. In (1) a photon is absorbed, leading to the LE state (2). Though internal conversion, the system can change to a CT state (3). By variation of the frequency, different characteristic time constants τ_{ET} can be measured,

which will answer question 1. From (3) there are three possible outcomes (green arrows). Dissociation can lead to the desired system of radicals (5). Through internal conversion the CT state can relax back into the ground state (question 2). Due to intramolecular vibrational redistribution the system may stay in a bound state (4) because the energy barrier can not be overcome (question 3).
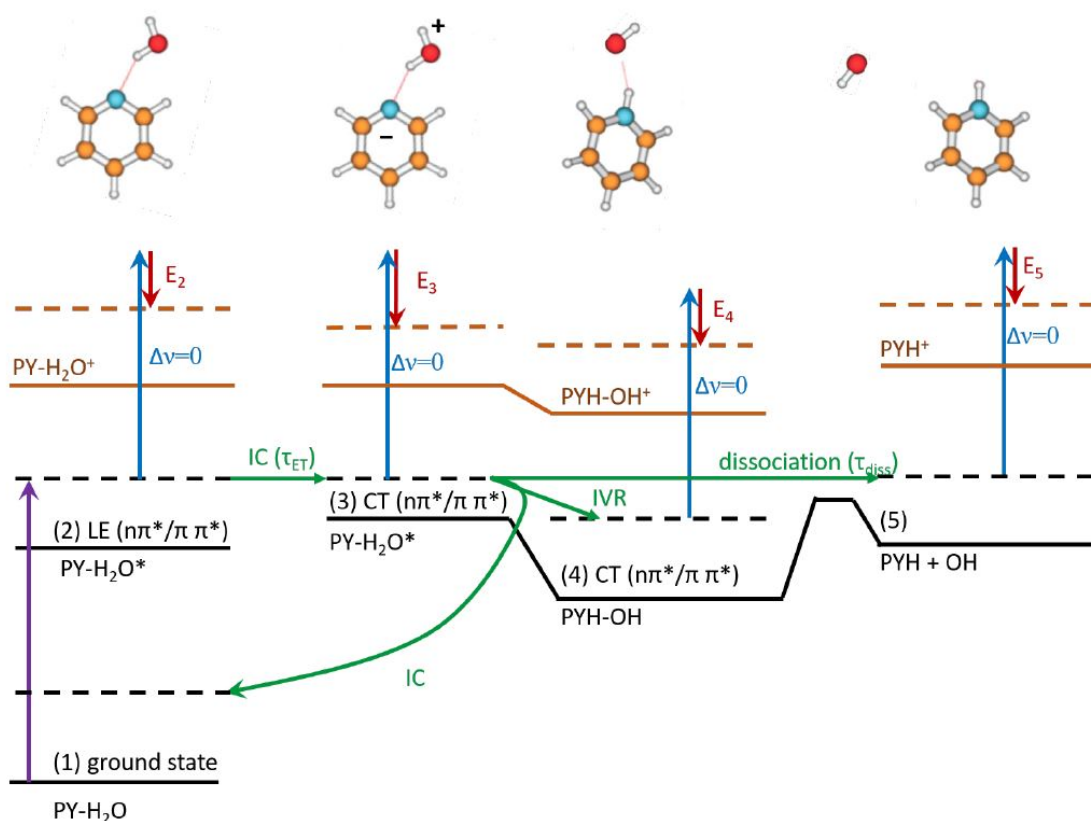

Figure 2.6: Kinetic model for water splitting with PY-H$_2$O

2.3.4 Coulomb explosion imaging (CEI)

Although the TU Graz will not concentrate on nuclear dynamics, the reader shall be provided in short with the principle of coulomb explosion imaging (figure 2.7). A pump-probe setup with 25 fs pump and 5 fs probe pulses will cause the investigated molecule to explode in the reaction microscope. The time of flight and the positions of the electrons
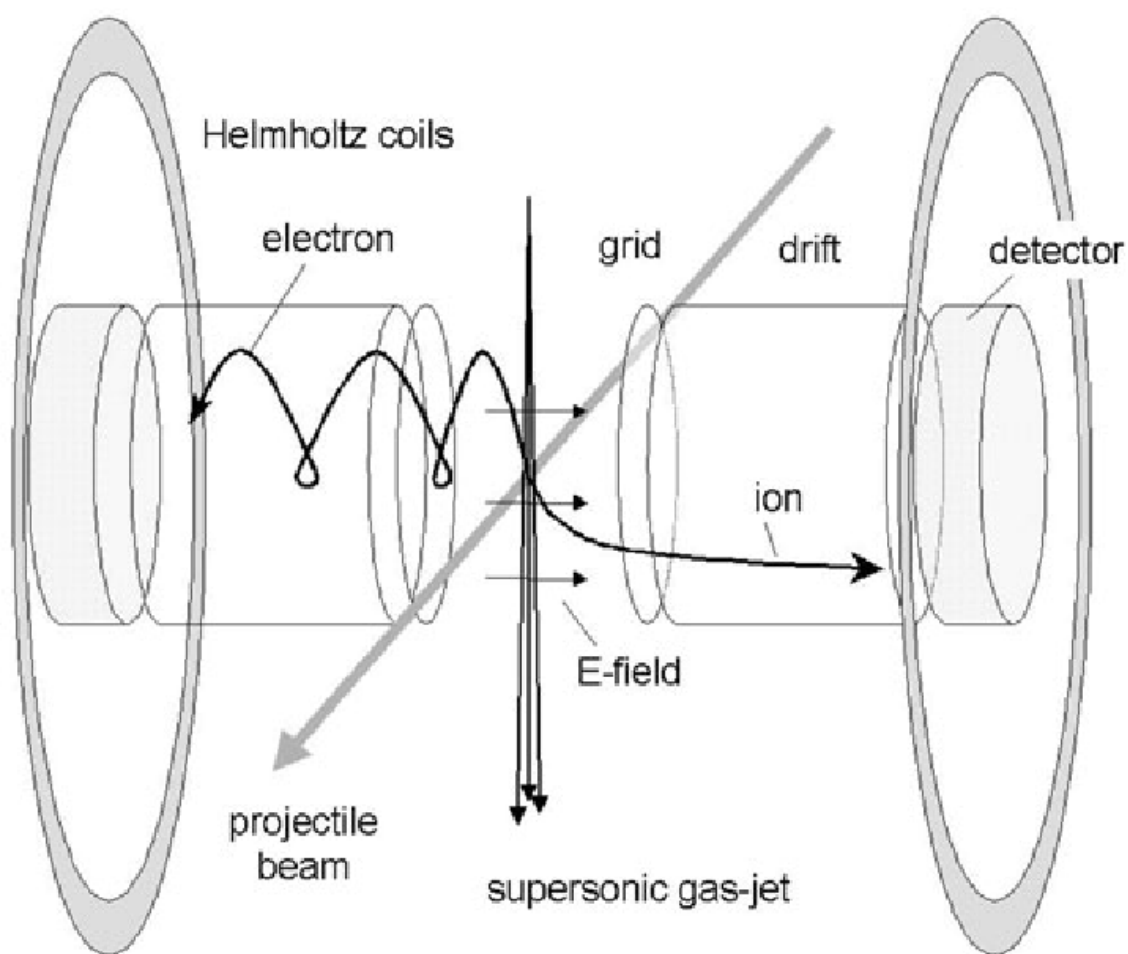
Figure 2.7: Principle of coulomb explosion imaging using a reaction microscope. Source: [41]

and the ions in coincidence are measured, which can be used to reconstruct the momenta of the fragments. This gives information about the structure right before applying the laser and leads to a high spatial resolution.

CHAPTER 3

Experimental Setup

To understand the EDPT process, both electron dynamics and nuclear structure changes have to be investigated. The ultrafast electronic structure dynamics will be investigated with the PEPICO method (explained in 3.1.1), whereas the ultrafast nuclear structure changes will be examined with the CEI method (described in 2.3.4) [25].

3.1 Optical Setup

The existing laser-system from the Femtolab I at the TU Graz will be used and the schematic optical setup is shown in figure 3.1. A Coherent Vitara oscillator and Legend Elite Duo amplifier with 4 mJ pulse energy and 3 kHz repetition rate is used (Titanium-Sapphire system delivering 25 fs pulses with 800 nm center wavelength). The laser output is split into a pump and a probe pulse with a variable pump-probe time delay. The pump pulses, containing about 60-80% of the laser pulse energy, will be frequency upconverted with an optical parametric amplifier (OPA). This system is a Coherent OPerA Solo (240 nm, 5.2 eV to 1600 nm, 0.8 eV). A prism compressor after the OPA allows to compress the pulses

to about 30 fs. The pulse duration and chirp can be measured by an existing frequency resolved optical gating (FROG) setup [27]. The laser beam then hits the molecular beam (green) in the main chamber perpendicularly and a time of flight spectrometer is used for detection (described in section 3.4.1).
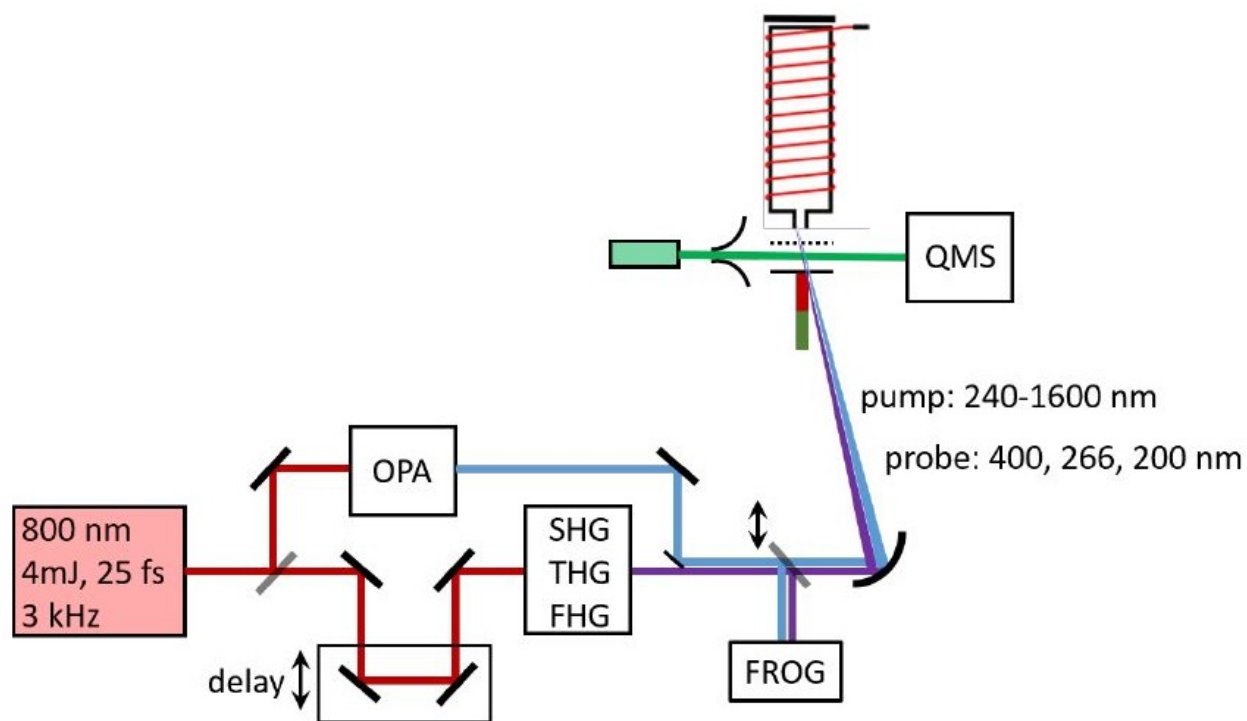

Figure 3.1: Schematic optical setup

3.1.1 PEPICO

In figure 3.2 the photoelectron (PE) spectrum and the photoion (PI) spectrum of acetone are shown. To obtain more information about the molecular system, the photo electron photo ion coincidence (PEPICO) technique can be applied.

Because the ions are heavier than the electrons, the electrons are first accelerated with a negative repeller voltage ($-3\,$eV has been a reliable value, like used in the Femtolab I). After detecting, the voltage is switched to a positive value (here: $+2\,$kV) and the
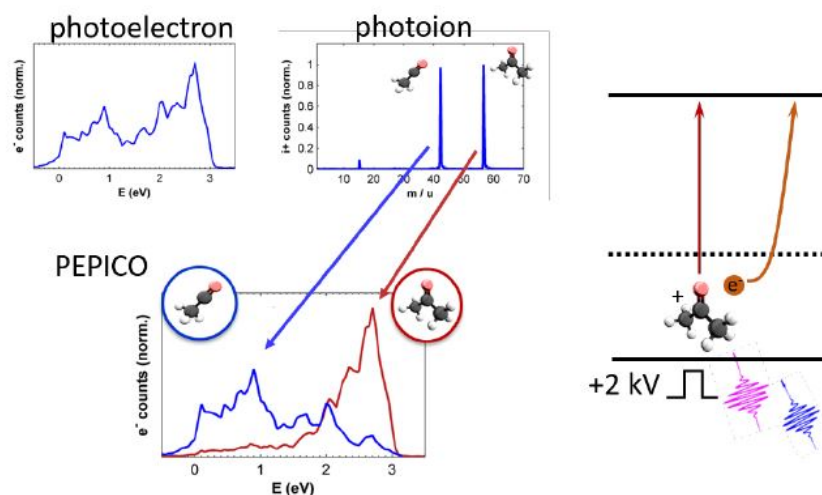
Figure 3.2: Schematic of TR-PEPICO. Left: PE and PI spectra together give the PEPICO spectrum which provides more information about the system. Right: successive acceleration of electrons and ions after pump-probe excitation/ionization

ions can be detected. In this way, more information can be obtained by assigning different parts of the PE spectrum to the parent (red) or the fragmented part (blue) of the investigated molecule. This technique allows to distinguish, if the fragmentation happens in the neutral molecule or if it is caused by the ionization. Therefore, it will be of significance for the H-detachment process. It also provides information about different cluster sizes due to the different masses and parallel relaxation pathways in a single molecule can be disentangled [22–24].

3.2 Setup Overview
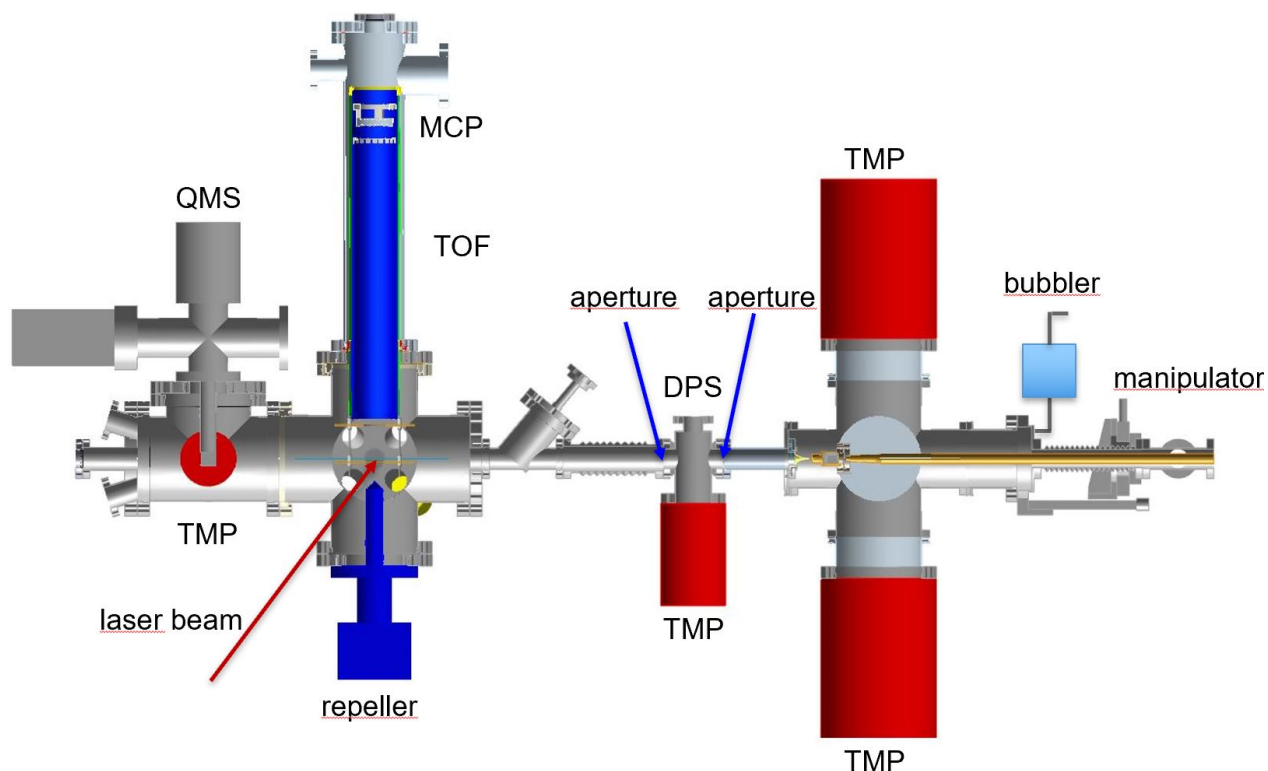
Figure 3.3: Overview of the apparatus (vertical cut) with components described in the text

The experimental setup of the seeded beam apparatus is seen in figure 3.3. The components will be explained in detail afterwards. Following the beam from right to left, the carrier gas He seeded with H_2O created with a bubbler enters the source chamber through an opening in the flange of the manipulator. On the far left of the manipulator the nozzle body is mounted that also contains the chromophore. The seeded beam then moves through a nozzle and skimmer into a differential pump stage (DPS) which is separated from the other chambers with 3 mm apertures (blue arrows). Then, the beam is perpendicularly targeted by the laser (red arrow) in the main chamber. The ionized system is then analyzed in a time of flight (TOF) spectrometer and detected with microchannel
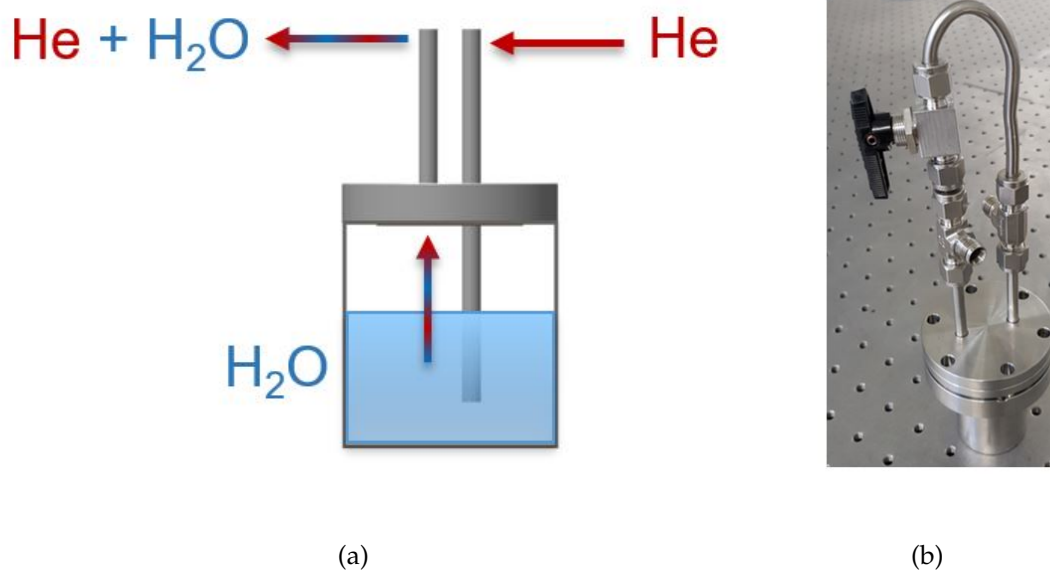
Figure 3.4: Schematic function of a bubbler (a) and photo (b)

plates (MCP) mounted on top of the TOF. Alternatively, the molecular beam can also be analyzed in a quadrupole mass spectrometer (QMS).

3.3 Source Chamber

3.3.1 Creating PY-$(H_2O)_n$ clusters

A bubbler (fig. 3.4(a)) is used to create a seeded beam consisting of He as carrier gas and water. He enters the small chamber that is filled with water (and later also other liquids like ethanol for AC and AO). The He rises and leaves the bubbler, seeded with a various number of H_2O molecules. The size of the H_2O clusters can be varied by changing the temperature of the bubbler by heating or cooling, thus changing the vapor pressure of the water. The valve in figure 3.4(b) is for bypassing the water and therefore flooding the whole system with inert gas, if necessary.
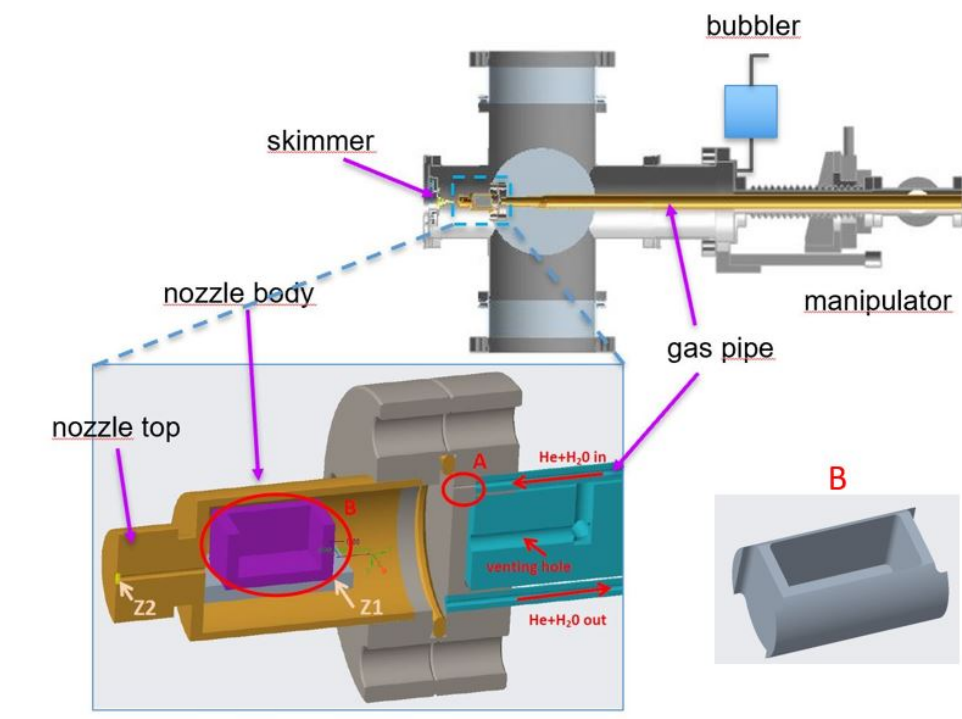
Figure 3.5: Source chamber (vertical cut) with manipulator without pumps and zoom on the nozzle body

In figure 3.5 the source chamber and the manipulator can be seen without the pumps. The He-$(H_2O)_n$ clusters created by the bubbler enter the chamber through a gas pipe. The nozzle body (yellow) is attached to the gas supply, exhaust and the holding pipe (cyan) via a flange. It is made out of copper to achieve high thermal conductivity and heat capacity. Within the nozzle body, the chromophore sits in the bowl (B, purple). The design of the bowl was altered to achieve a more stable setup (right, bottom). Through the small opening (A) the gas enters and is mixed with the chromophore. This opening is small to have a higher flow rate and to prevent the chromophore to diffuse back into the supply and condense there. The beam then leaves the chamber through the 30 µm palladium-iridium-nozzle (Z2), undergoing an adiabatic free jet expansion [16,28]. This supersonic expansion into vacuum leads to a cold, nearly mono-energetic seeded beam. This has been

successfully used to produce PY-$(H_2O)_n$ clusters [13] and also similar clusters [15]. The beam then leaves the source chamber through a 400 µm skimmer. To obtain a very small distance between skimmer and nozzle, the nozzle was designed to be as flat as possible. The manipulator is mounted on a stage that can be moved in x,y and z directions for optimizing the seeded beam flow.

3.3.2 Heating

The nozzle top has to be the hottest part of the nozzle body to avoid condensation and therefore blocking. In figure (fig. 3.6) four OMEGA KHLVA rectangular heating bands (table 3.1) were applied to the nozzle parts and the holding pipe and are held by metal clamps. Their label from left to right is 'nozzle top', 'nozzle body', 'nozzle flange' and 'HB rod'. The same labels will be used in the measurements (section 4). On each clamp a thermocouple was attached.
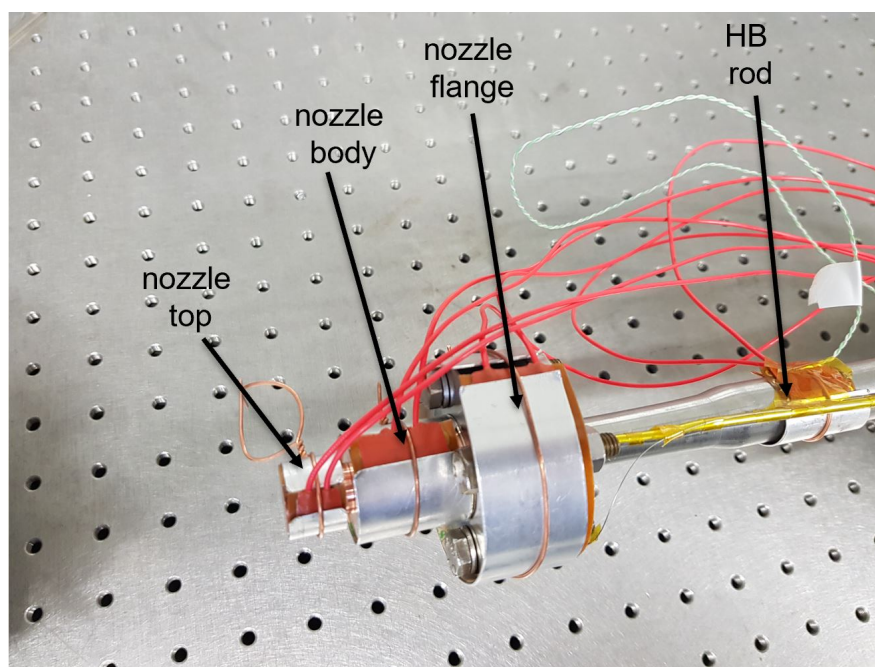
Figure 3.6: Positions and labels of the heating bands and the thermocouples used on the nozzle body

Table 3.1: Product names and dimensions of the used nozzle heating bands from OMEGA

name	width / cm	length / cm	power / W
KHLVA 102-10-P	2.5	5	20
KHLVA 103-10-P	2.5	7.6	30
KHLVA 105-10-P	2.5	13	50
KHLVA 0502-10-P	1	5	10

The maximum voltage of the heating bands is 28 V and the maximum temperature is 149°C. To achieve a maximum heating power, a controller circuit was designed and built (figure 3.7). The heating elements have different resistances that can be adjusted by the potentiometers R, leading to a different base current on the transistors T controlling the currents over the heating elements. This allows to control the heating of the whole system with only one thermocouple T1 at the first element (nozzle top), prevents overheating and ensures that the nozzle top is the hottest part of the system. R_{Wire} is for heating the gas supply tube which is described below. The blue dashed line symbolizes the vacuum chamber, where the heating elements are situated. The red dashed line symbolizes a box where all controlling elements are placed. The sources V_1 and V_2 are on the same positive potential. Source V2 supplies the heating elements (R_{H1} to R_{H4}) and the series resistors (R_1 and R) with 0 to 28 V. Due to the different minus voltage at Source V_1, the voltage of R_{wire} can be adjusted. A PID controller (Eurotherm 2116) measures the temperature of the first heating band (R_{H1}) and controls source V_2. Due to the different resistances of the heating bands, the potentiometers R are 1-10 kΩ to apply the same power. If the Base-Emitter-Voltage is estimated with 0.7 V, the maximum power consumption at R1 is

$$P_1^{max} = \frac{(U_2 - U_{BE,T1})^2}{R_1} = \frac{(28 - 0.7)^2}{1000} = 0.75 \text{ W}$$

which can't be applied on a single small standard resistor that can only handle about 0.25 W. That is why four parallel 4 kΩ resistors were used. All the R and R1 are situated on
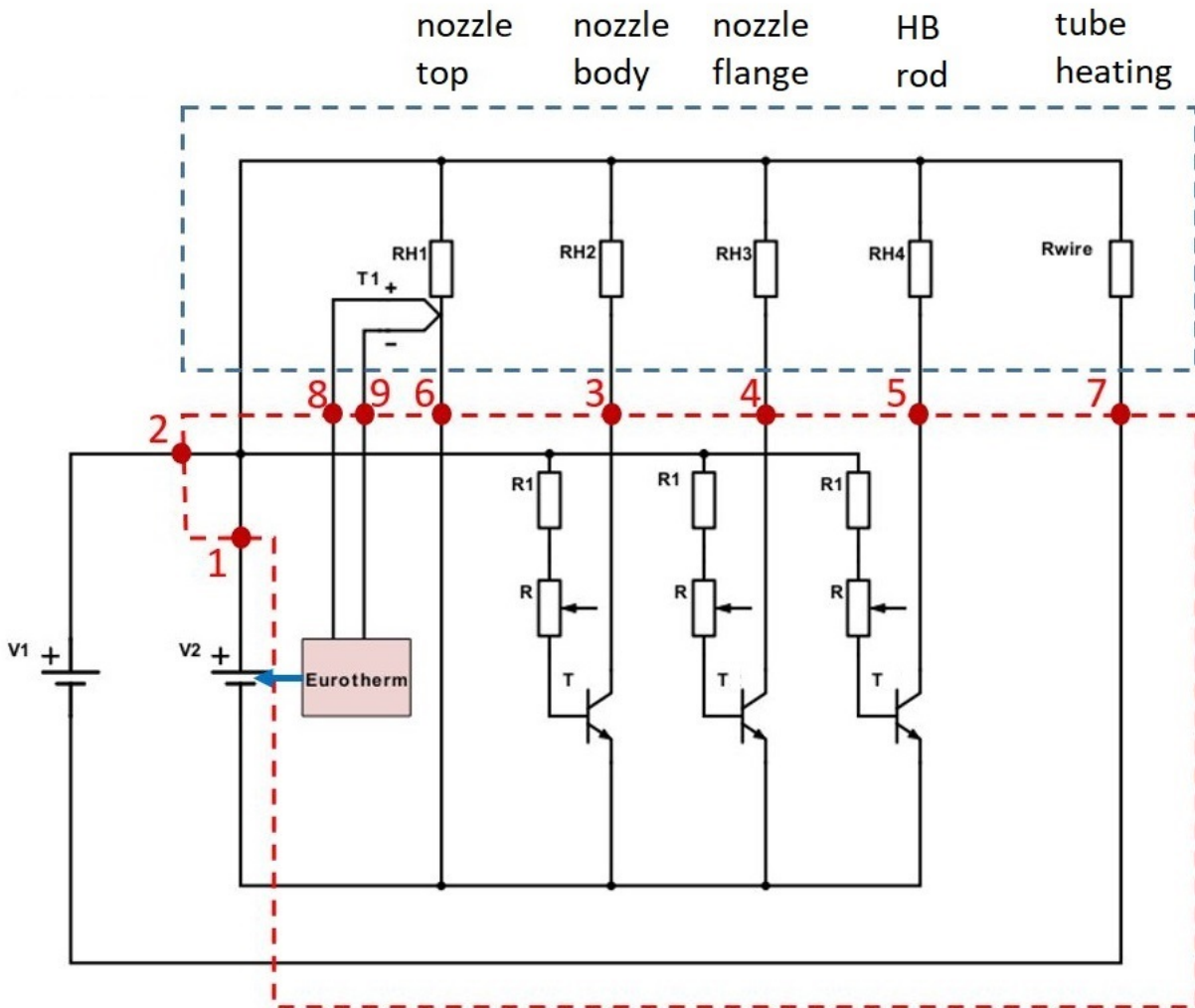
Table 3.2: Part list of the transistor circuit

name	description	comment
R1	series resistors	4 parallel $4\,\mathrm{k\Omega}$
R	potentiometers	for adjusting the current in that path
T	power transistors	DB239C
Eurotherm	temperature controller	Eurotherm 2116
V1	voltage source	V1+ is connected to V2+
V2	voltage source	V2+ is connected to V1+
T1	thermocouple	
RH1	heating band nozzle top	KHVLA polymide film flexible
RH2	heating band nozzle body	KHVLA polymide film flexible
RH3	heating band nozzle flange	KHVLA polymide film flexible
RH4	heating band nozzle HB rod	KHVLA polymide film flexible

a board. Three power transistors (DB239C) are used which allow currents up to 2 A and have a gain of about 100. Assuming a current of >1 A per heating band, the maximum current is estimated ~ 5 A. To avoid overheating of the transistors, they were mounted on a cooling rib.

Differently from the data sheet, the PID controller has 14 V at the logic exit. An additional potentiometer (not shown in figure 3.7) was installed to ensure a maximum of 28 V (R_{PID} in figure 3.8(a)) output at V2, corresponding to 8.75 V output at the PID controller. The components are listed in table 3.2.

Table 3.3 and 3.4 show the sub-D ports of the thermocables and the heating bands (HB). The sub-D at the chamber are male and the description in the tables is the female connection. Because the grounds are connected to save ports, the temperatures have to be

Figure 3.7: Controller circuit for nozzle heating with parts described in table 3.2. Red dots are the ports for serial communication. Explained in table 3.3
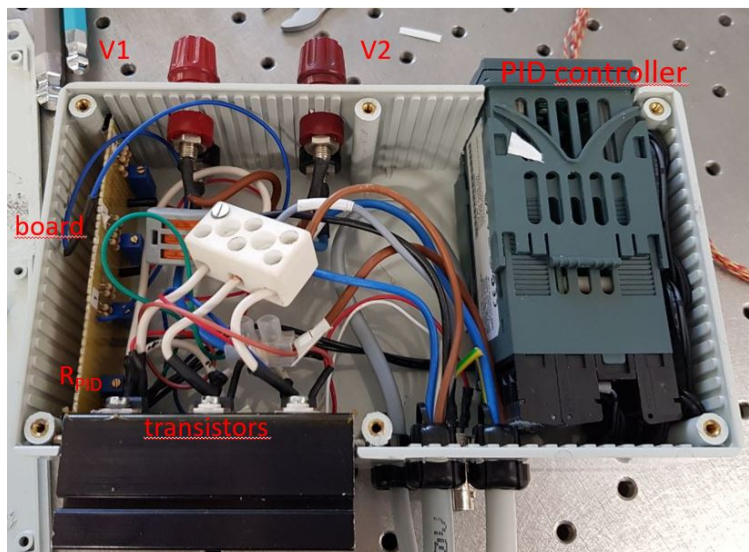
(a)
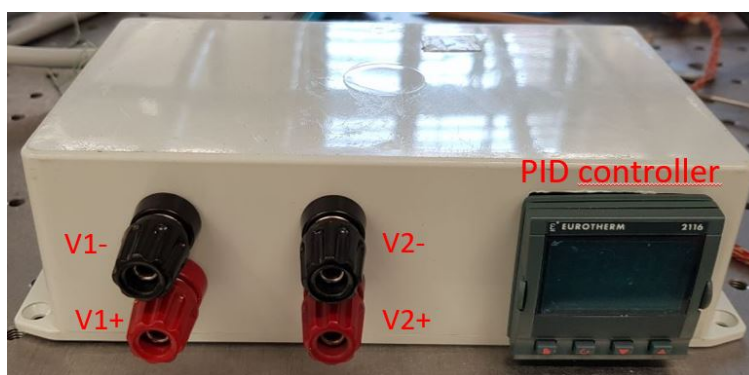
(b)
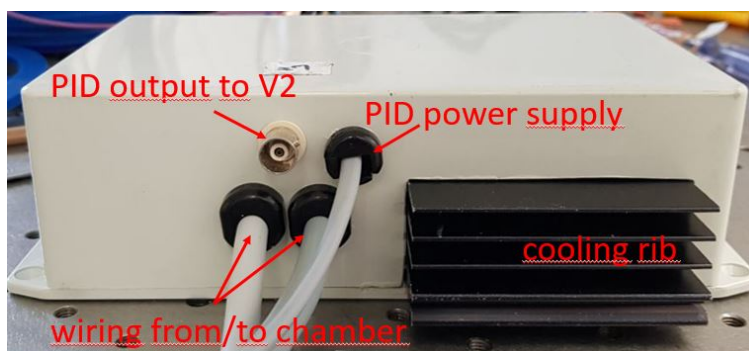
(c)

Figure 3.8: Photos of the transistor controller circuit open (a), front (b) and back (c).

Table 3.3: Serial sub-D ports of the heating bands into source chamber.

i ... Pin number

i	description	color
1	0...28 V V_2+, controlled by Eurotherm 2116	blue
2	0...28 V V_1+, connected to 1	blue
3	HB nozzle top from chamber to V_2-	brown
4	HB nozzle to collector T_1	black
5	HB nozzle to collector T_2	grey
6	HB nozzle to collector T_3	blue
7	HB coil from chamber to V_1-	brown
8	HB nozzle top +	yellow
9	HB nozzle top -	red
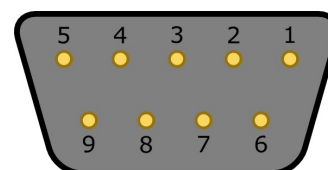
read seperately - otherwise, the signal is wrong!

The high pressure gas supply is actually coiled spirally around the manipulator as shown in figure 3.9 to allow the stage to move. There has to be a temperature gradient to prevent the water from condensing in the supply. Therefore, the supply has to be heated with a tungsten wire. Because it is suitable for ultra high vacuum, kapton tape was used (orange and yellow) between the tube and the wire for electric isolation. The supply tube was only covered half with the kapton to avoid air pockets, respectively virtual leaks. The yellow parts are just for keeping the wire attached to the tube and are in 2-3 cm distance from each other.

To examine the temperature distribution of the heated tube in vacuum, an infrared camera was used (shown in fig. 3.10). Tungsten wire was mounted on a model pipe, put in a chamber and IR pictures were made. The chamber was evacuated to 2.2×10^{-1} mbar and 1 A was applied to the wire. Taken the fact that kapton radiates dif-

Table 3.4: Serial sub-D ports of the thermocouples into source chamber.

i ... Pin number

i	description	color
1	HB rod middle	red
2	pipe in middle	red
3	HB rod	red
4	HB nozzle body	red
5	HB nozzle flange	red
6	ground (yellow)	red
7	ground, connected to 6	yellow
8	not connected	-
9	pipe coil	red
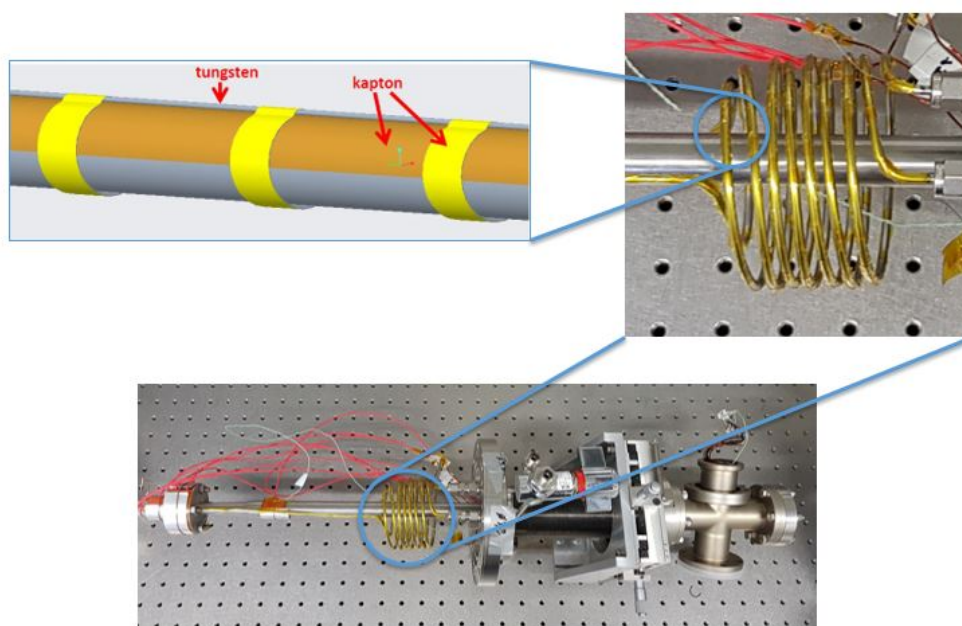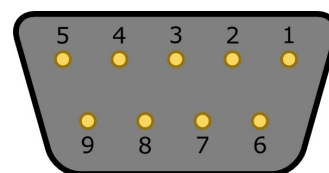
Figure 3.9: Bottom: photo of the manipulator. Top right: zoom on the high pressure gas supply and heating. Top left: drawing of the tungsten wire pressed on the gas tube with kapton
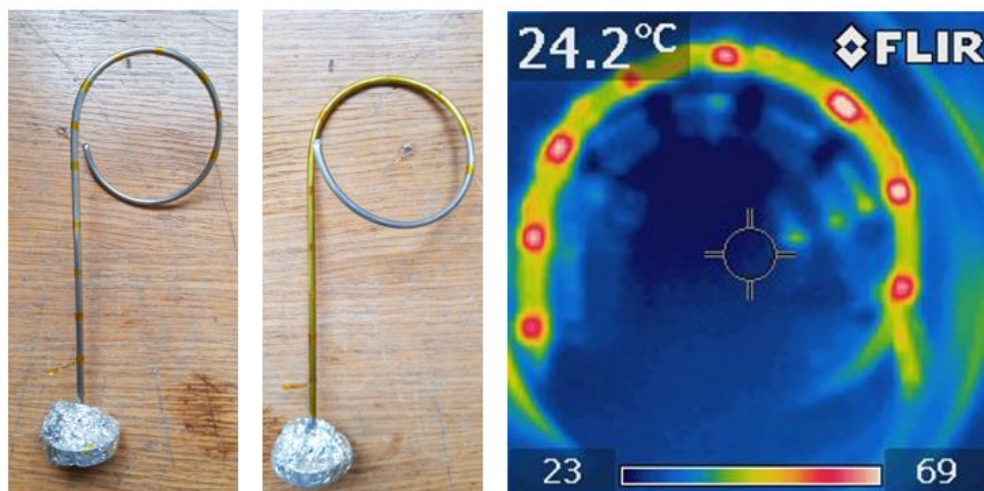
Figure 3.10: Model pipe for IR heating experiment. Front of pipe (left), back (middle), IR picture in chamber (right).

ferently from metal and that the red and white parts in the picture are the parts where the wire is pressed down, a homogeneous heating was measured. The right picture was taken through a looking glass and the artifacts inside are reflections in the chamber.

3.4   Main Chamber

3.4.1   Time of flight (TOF) spectrometer

The time of flight spectrometer was designed similar to the existing in the Femtolab I [34] with a magnetic bottle setup. In figure 3.12 the TOF and its components are shown. After ionizing the molecular beam, the repeller accelerates the charged particles towards the MCP. For PEPICO, a high voltage switch changes the negative voltage for electrons to a positive one for ions. For the new setup, however, the existing setup in the Femtolab I was improved by adding a third plate for spatial focus, which is called Wiley-McLaren-Setup (figure 3.13) with a two-stage acceleration field [33]. Here, the geometry as well as the applied voltages both contribute to a better spatial focus. The far left plate is called repeller,
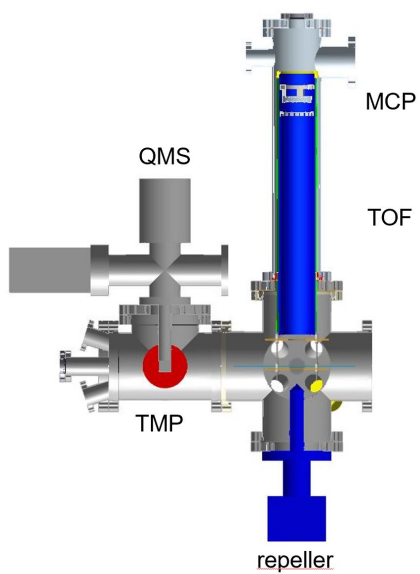
Figure 3.11: Main chamber (vertical cut) consisting of QMS, repeller and TOF
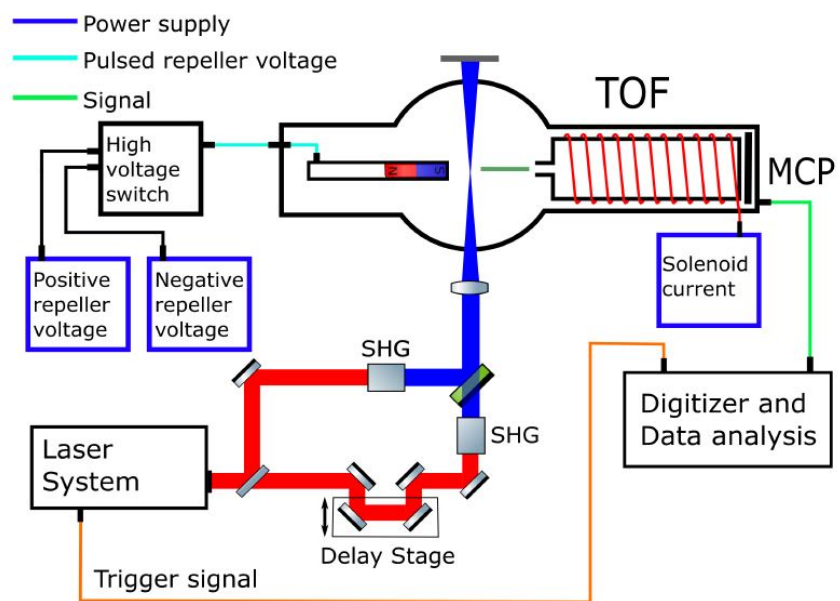
Figure 3.12: Schematic of Time-of-Flight Spectrometer. Source: [35]
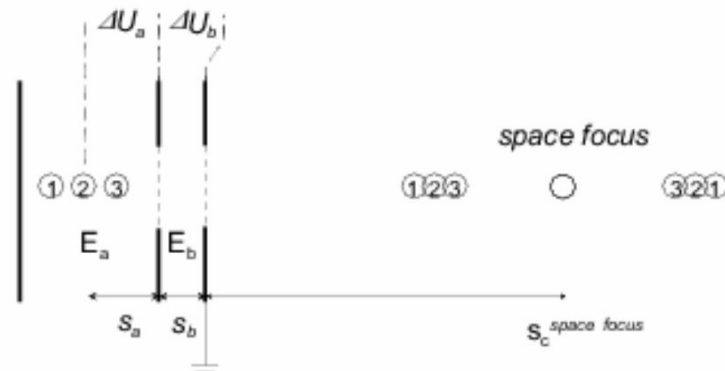
Figure 3.13: Schematic Wiley McLaren setup with a two-stage-acceleration field. Source: [32]

the middle extractor and the right one ground. There should always be a voltage gradient from left to right to achieve an acceleration. It has been approved that for electrons, the repeller voltage is at $-3\,$V and for ions at $2\,$kV. By variation of the voltages, different signals were investigated (sec. 4.4).

The new setup was simulated with ions using SIMION (fig. 3.14). SIMION is a software to calculate electric fields and the trajectories of charged particles in those fields. Because the voltage ratio of extractor and repeller is very important, figure 3.15 shows the mean flight time over the standard deviation $\frac{\bar{t}}{\sigma(t)}$ as a function of the voltage ratio $\frac{V_{ex}}{V_{rep}}$. At a certain ratio, the standard deviation $\sigma(t)$ shows a minimum and therefore the resolution indicates a maximum.

3.4.2 Microchannel plate (MCP)

The principle of a chevron MCP is seen in figure 3.16. An electron is accelerated by the repeller to the MCP front. If there is a potential difference between MCP front and MCP back, further acceleration leads to secondary electrons (red) and to an avalanche effect that can be detected.

The MCP for this setup is a Detection Quality Long-Life Microchannel Plate Set (MCP 40/12/10/8 D 60:1 27-79UA, MS) chevron MCP from PHOTONIS (fig. 3.17). This
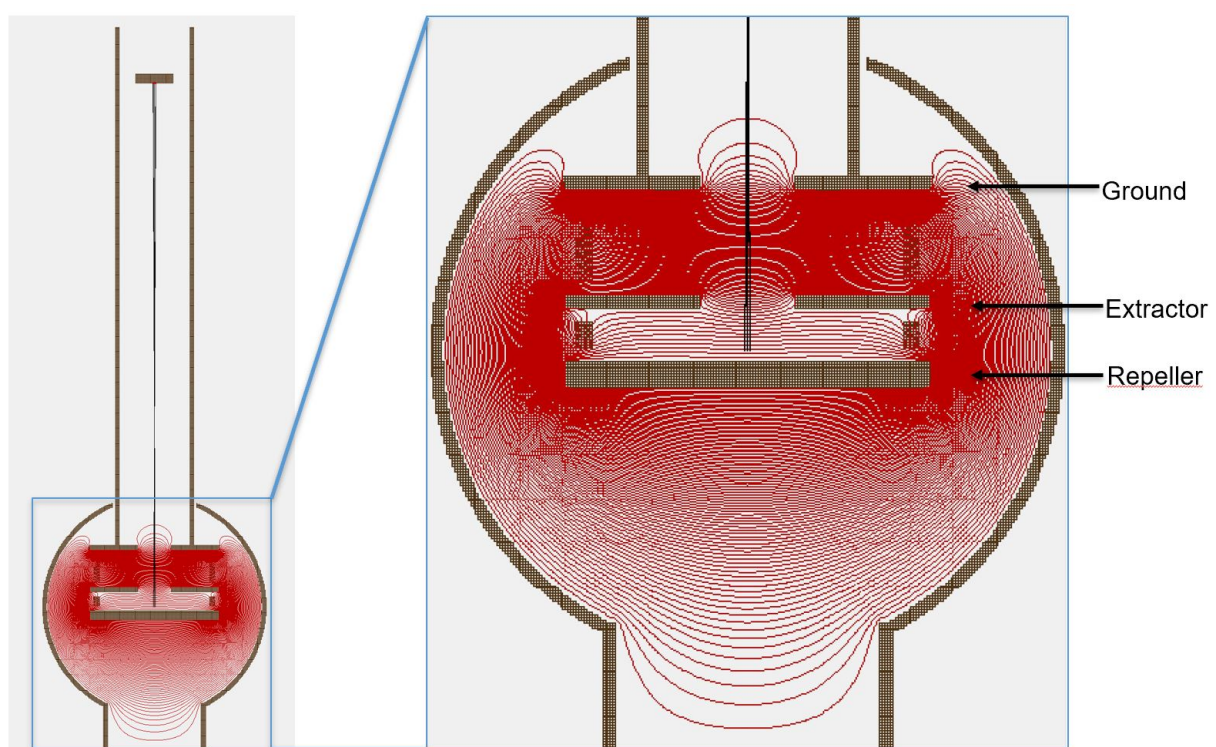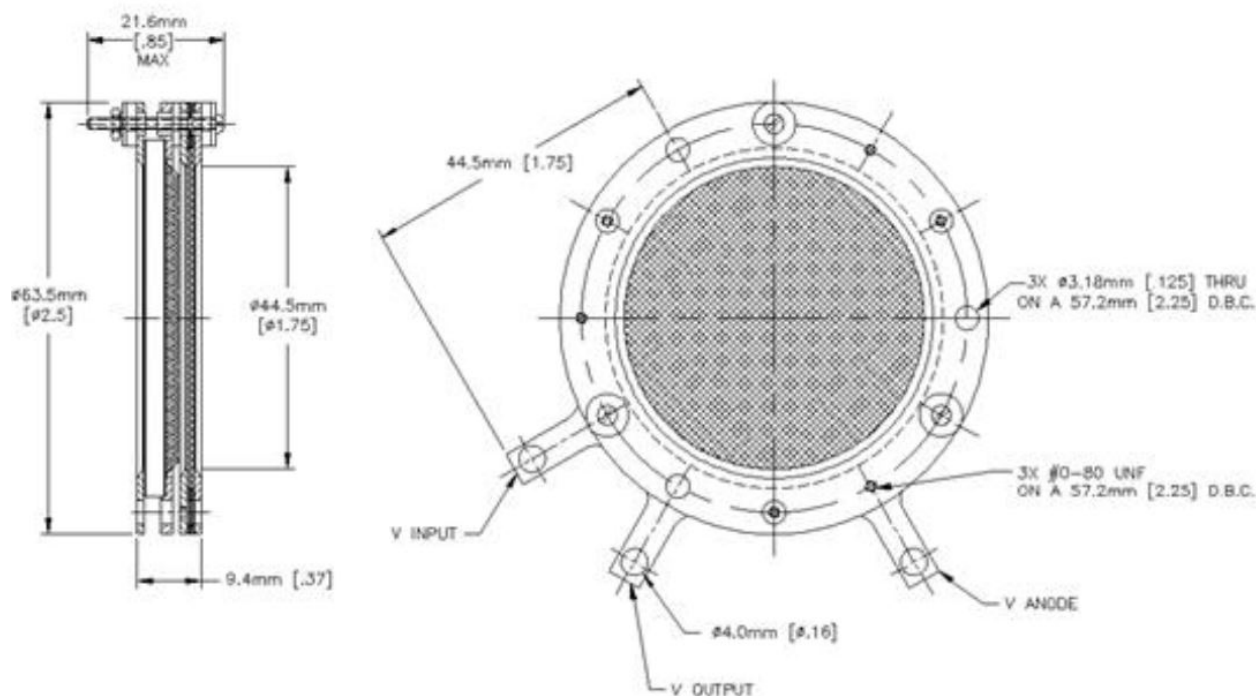
Figure 3.14: Simulated electric fields in the TOF tube with ion trajectories and zoom on the important region of the fields near the plates. Source: SIMION
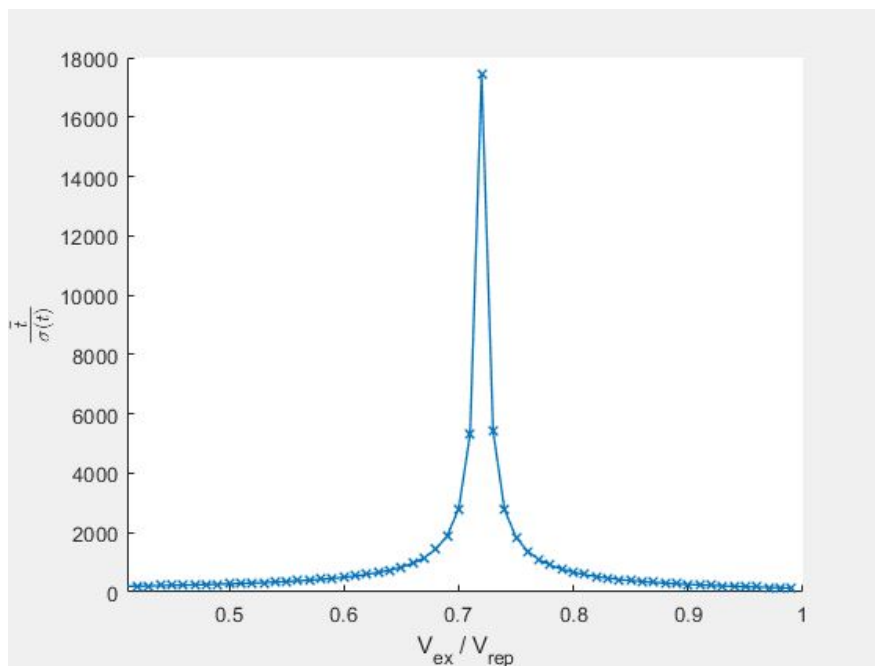
Figure 3.15: Simulated mean time of flight over standard deviation versus extractor voltage over repeller voltage. Source: SIMION
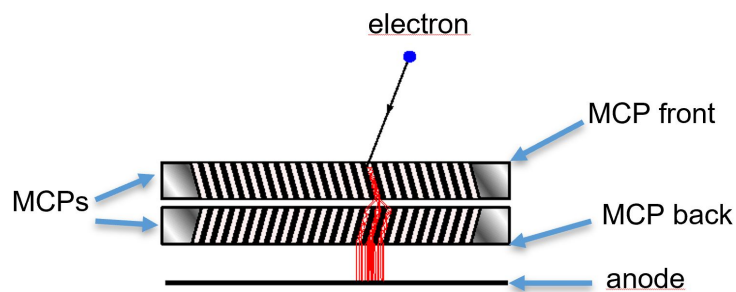
**Figure 3.16:** Schematic of a chevron MCP. Source: adapted from [40]

Figure 3.17: Dimensions of the MCP. Source: PHOTONIS

is an exact copy of the existing MCP in the Femtolab I, however, only the plates were obtained and self-assembled and the detector was also self-made.

3.4.3   Quadrupole mass spectrometer (QMS)

The QMS will be shared with the Femtolab I and is described in [36] on page 20. Because the first measurement was rather in the beginning, there are still many carbonates (figure 3.18). Everything seemed to work fine, but the QMS was needed in the other lab shortly after this measurement. However, a plug and play was successfully tested and a change between the laboratories won't take long. Analyzing the spectrum, there is some hydrogen (u=1 or 2 for molecular hydrogen), water (u=18), molecular nitrogen and/or carbon monoxide (u=28), followed by further carbon oxides around u=42, 55 and 70. This contamination can and will be improved by baking out the chambers.
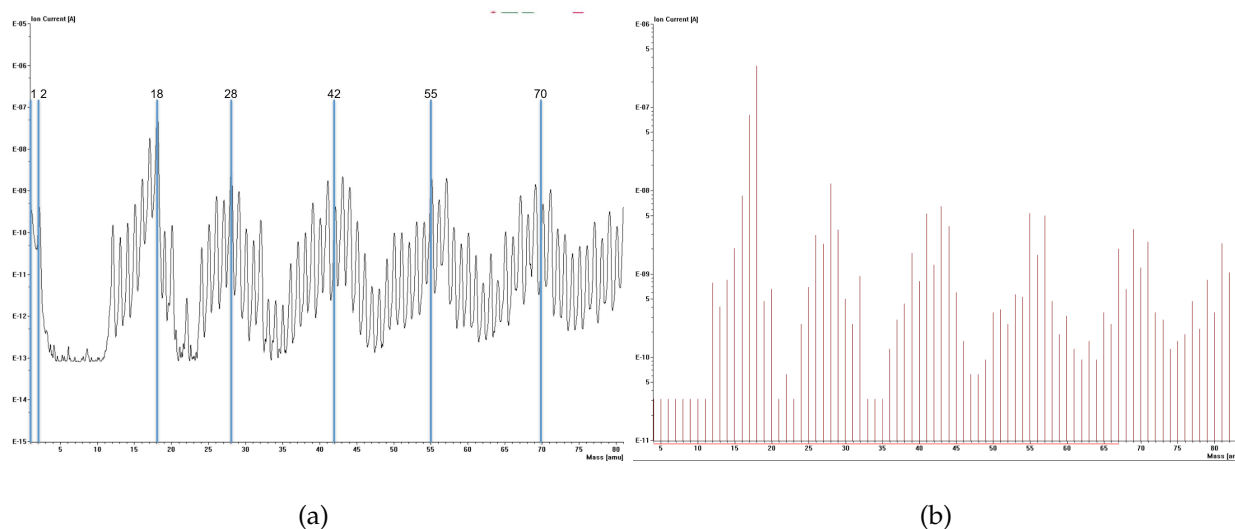
Figure 3.18: First scan with the QMS with characteristic carbon hydrogen molecules. Analog scan (a) and bargraph (b)

3.5 Pumps

In figure 3.19 the turbomolecular pumps and their suction powers for He are shown. There are two pumps on the source chamber (LEYBOLD Turbovac361 and PFEIFFER TMH521), to allow for higher nozzle pressures. In the DPS a PFEIFFER TMU065 with a low suction power in comparison is sufficient. The main chamber pump (PFEIFFER HiPace300) was mounted off-axis to allow a viewport in beam direction at the far left end. The power is sufficient for the chambers as will be described in section 4.2. The pre-vacuum pumps are two rotary vane pumps, one for the main chamber (PFEIFFER BALZERS DUO 008 B) and one for the source chamber (VARIAN CD-700). The pipe diameter of an ISO-K 40 for the main chamber was sufficient. For the source chamber two ISO-K 50 were used. The pre-vacuum pumps are equipped with a ceolite trap for oil filtering which can be baked out for cleaning. The heating bands for bakeout are mounted to achieve a best possible homogeneous heating of the main chamber and the DPS and are

covered with aluminum foil. Underneath the foil, thermocouples are situated to prevent an overheating at all times, attached with kapton tape to exclude short circuits.

ATTENTION AND POSSIBLE DANGERS

- There is only an aperture and no valve between the SC and the DPS, which should be considered when pumping down or venting. To prevent the skimmer from being damaged, obey the following procedure for venting the system and backwards for pumping down:

  1. close valves between MC prevac pump and DPS pump
  2. close valve at the DPS pump
  3. close valves between SC prevac pump and the SC pumps
  4. connect bulk from the DPS pump to the SC prevac pump and open valve to have prevacuum from the SC prevac pump
  5. switch off SC and DPS turbo pumps
  6. to avoid oil flow when venting, make sure that the SC prevac pump is still running and the valve at the SC prevac pump is closed
  7. the system can now be vent

- The maximum bakeout temperature for the flanges at the turbopumps is $120°C$ with water cooling. According to [34] on page 35, 2.5 days of baking out is sufficient to achieve 1×10^{-10} mbar, however, the first bakeout should be supervised with the thermocouples.

- When in operation, a water cooling has to be turned on. To detect water leaks, two humidity sensors were placed on the ground which can lead to a loud signal when the floor gets wet. Also, a flowmeter was installed as an additional monitoring.
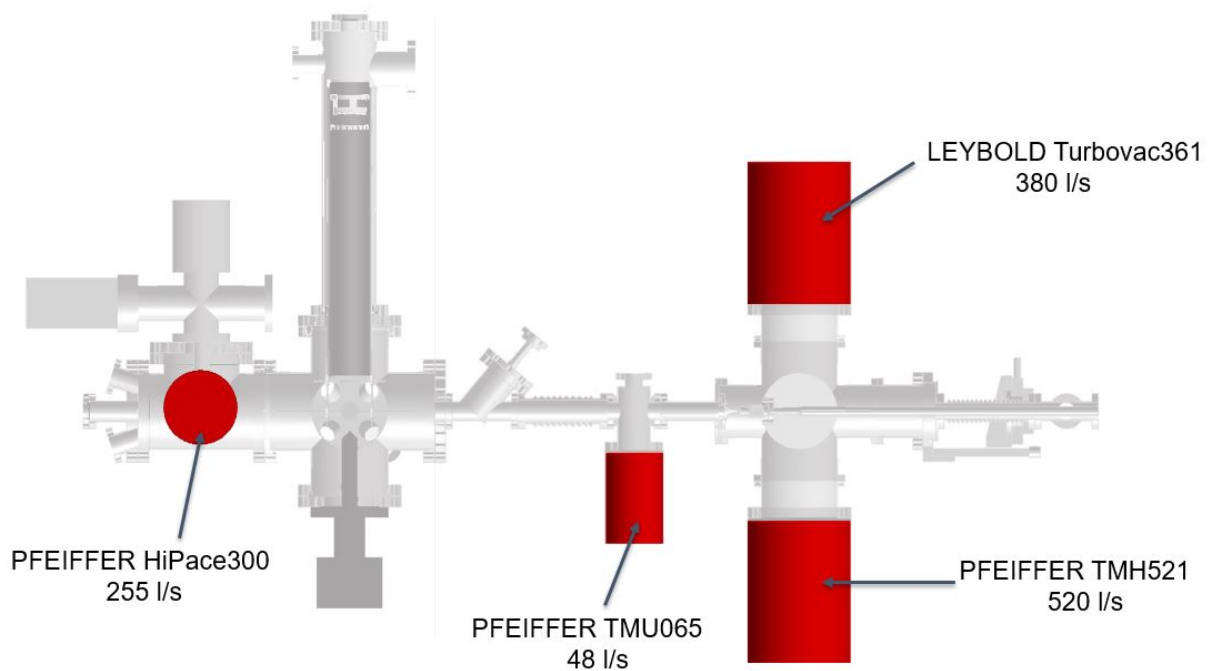
Figure 3.19: Turbomolecular pumps and their suction power (for He).

To estimate a base pressure in the source chamber that depends on the He pressure, the following equation (taken from equation 1.14 on page 18 in [37]) was used. The suction power of both SC pumps together is $900\,\mathrm{l\,s^{-1}}$ or $0.9\,\mathrm{m^3\,s^{-1}}$. The estimated pressure

dependence is shown in figure 3.20.

$$p = \frac{R \cdot T}{M \cdot S} \cdot P_0 \cdot \frac{d^2 \pi}{4} \cdot \sqrt{\frac{\kappa \cdot m_{He}}{k_B \cdot T_0} \left(\frac{2}{\kappa + 1}\right)^{\frac{\kappa+1}{\kappa-1}}}$$

R ... gas constant ($8.314\,459\,8\,\text{kg}\,\text{m}^2\,\text{s}^{-2}\,\text{mol}^{-1}\,\text{K}^{-1}$)

T_0 ... temperature in source chamber (for estimation take environmental T = 300 K)

T ... environmental temperature (300 K)

M ... mole mass He ($4.002\,602\,\text{g}\,\text{mol}^{-1}$)

S ... suction power ($0.9\,\text{m}^3\,\text{s}^{-1}$)

P_0 ... pressure in source chamber (1 bar to 4 bar)

d ... nozzle diameter ($30\,\mu\text{m}$)

κ ... heat capacity ratio ($\frac{5}{3}$)

m_{He} ... mass of He ($6.646\,476\,4 \times 10^{-27}\,\text{kg}$)

k_B ... Boltzmann constant ($1.380\,648\,52 \times 10^{-23}\,\text{J}\,\text{K}^{-1}$)

(3.1)

Because the pumps were used and contaminated with oil, they had to be cleaned. Therefore, a successful bakeout was made. In figure 3.21 one of the pumps is seen and figure 3.22 shows the QMS signal before and after bakeout of one of the pumps. The allowed maximum temperature of the high vacuum flange was 120°C and 90°C for the rotor according to the manual. Therefore, four thermocouples were used to ensure overheating and damaging the turbopump. The middle part of the pump was around 80°C. First, at 2-4 there is He. At 18 u there is H_2O and at 28 there is N_2.The most relevant elements are the hydrocarbons around 30 u and 40 u. Figure 3.22(b) shows the signal after a two day bakeout. Here the hydrocarbons practically vanished and only some H, H_2, H_2O and
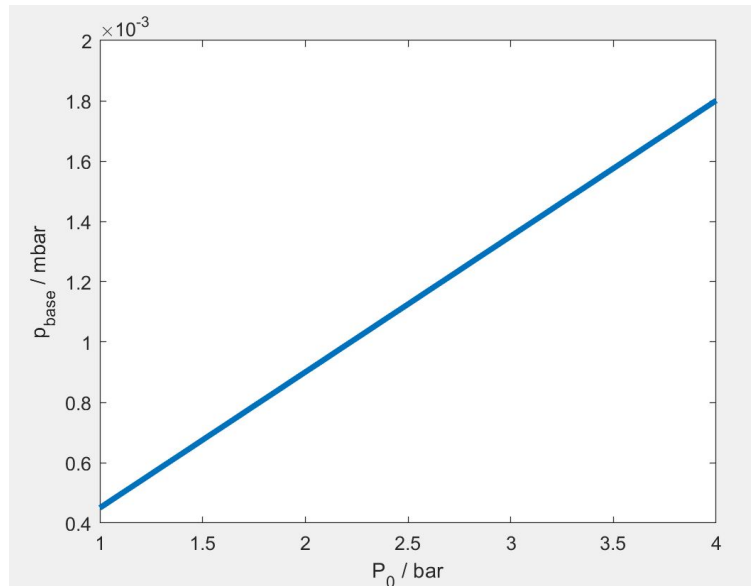
Figure 3.20: Calculated dependency of He gas pressure and SC base pressure.

N_2 remained. The used QMS (not the one connected to the main chamber) showed some problems. For example, after a continuous measurement of 30 min an error occurred. After shutting it down and wait for a proper cooldown, it was possible to activate it again. This could be improved by a better working QMS. There seems to be much more signal in the beginning than in the end, however, the pressure displayed on top is only a third. Although this can't be true, a trend was identified and the pumps worked fine afterwards (see sec. 4.1).

3.6 Pressure gauge

There are two pressure gauges connected to each the main chamber and the source chamber (PFEIFFER PKR261 compact full range pressure gauge). The gauge is calibrated for air. According to the manual, the effective pressure has to be calculated (equation 3.2)
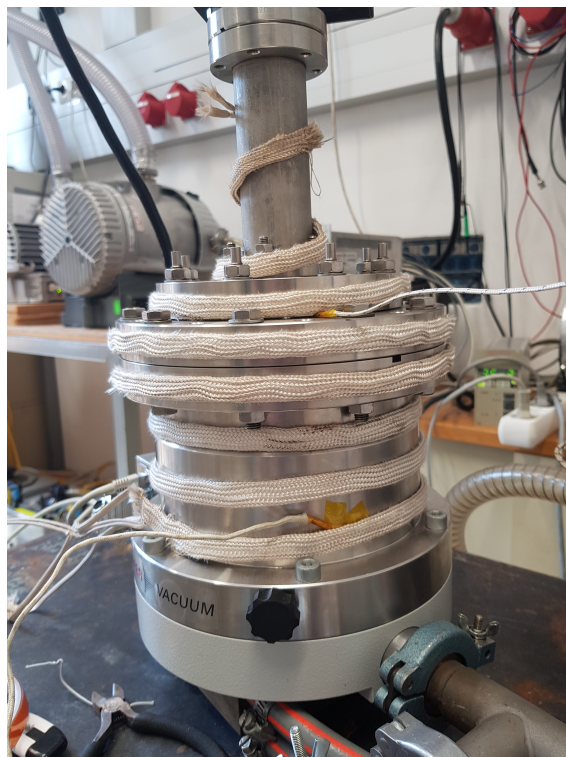
Figure 3.21: Photo of turbomolecular pump bakeout.

(a)

(b)
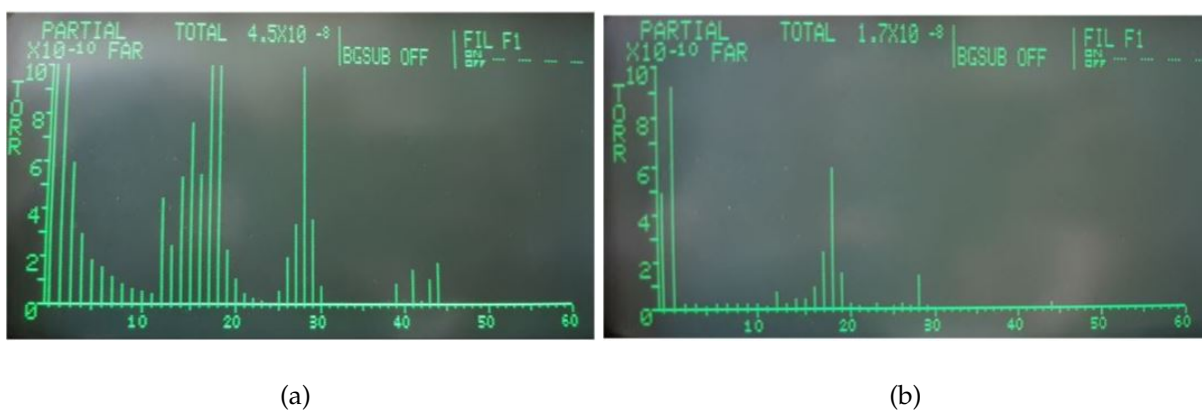
Figure 3.22: QMS signal before pump bakeout (a) and after two days (b).

(a)   (b)
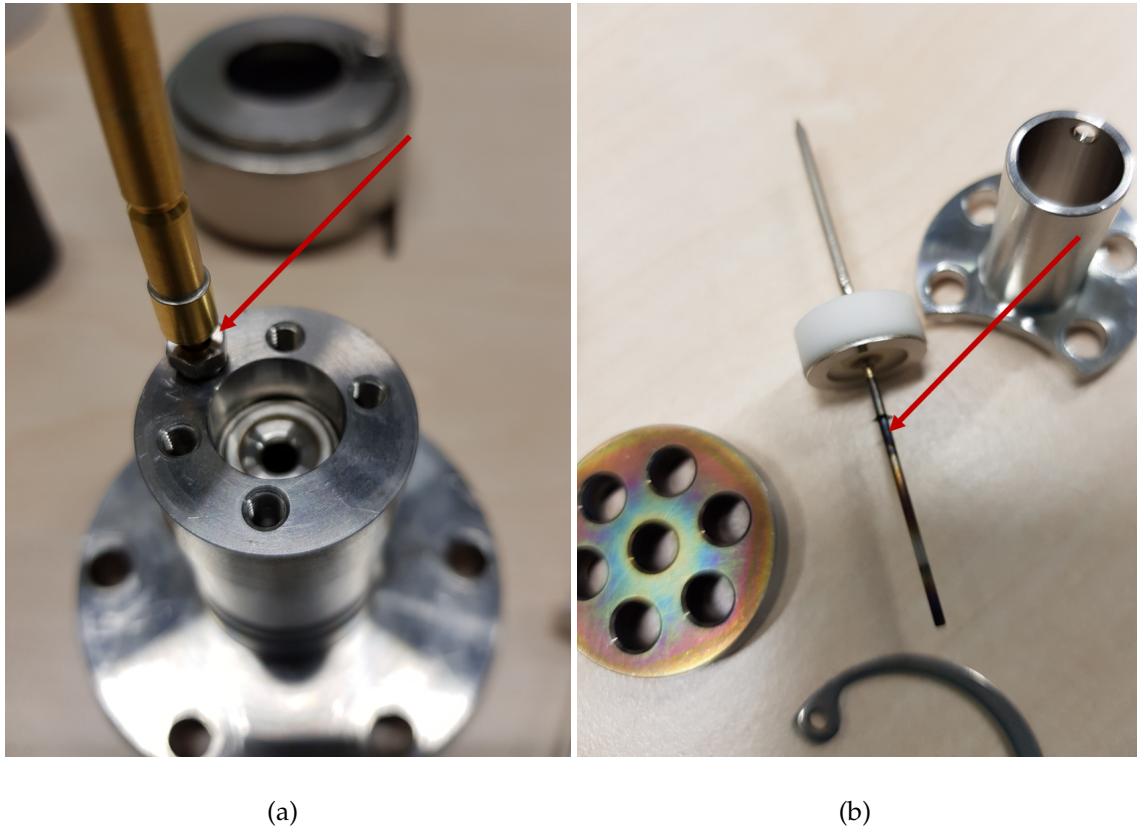
Figure 3.23: Disassembled PFEIFFER compact full range pressure gauge.

with an average linear factor K which is $K_{He} = 5.9$ for helium.

$$p_{eff} = K \cdot p_{indicated} \tag{3.2}$$

One of the pressure gauges indicated a leak at the pirani element. A two-component glue (TORRSEAL vacuum epoxy) was used to fix the pirani (red arrow in 3.23(a) and (13) in 3.24). The given mix-ratio of mass 100:44 was obeyed and the parts were baked out for two hours at 80°C. Also the anode (red arrow in 3.23(b) and (10) in 3.24) was cleaned with acetone. After a recommended three-day-cure, the gauge showed no leak at all anymore.
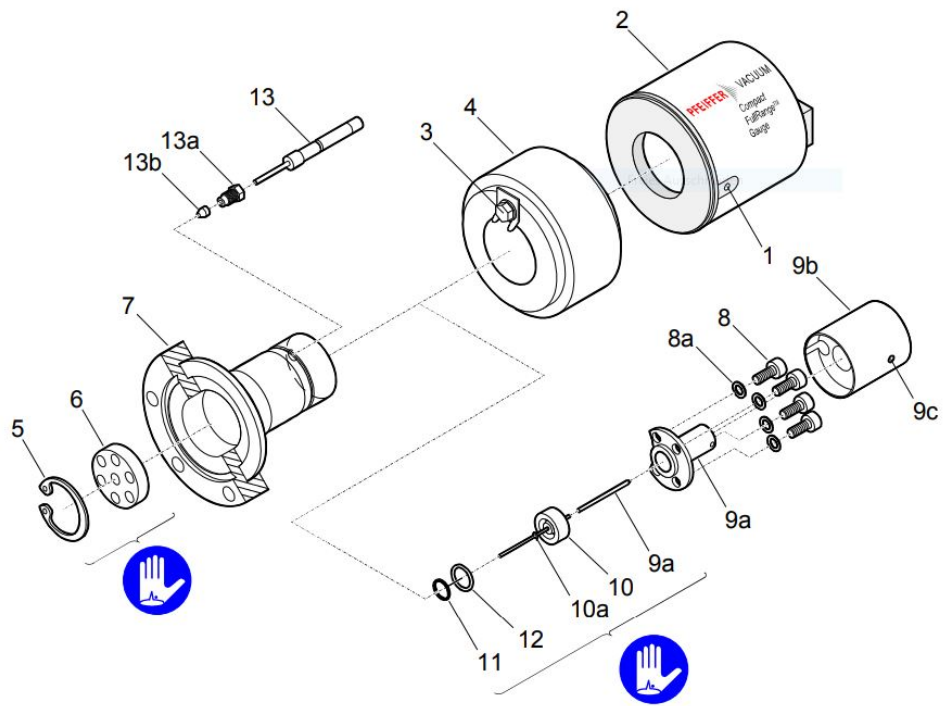
Figure 3.24: PFEIFFER compact full range gauge manual. Source: [29]

CHAPTER 4

Results

After describing the parts of the setup, this section provides with preliminary and characterization measurements. First, vacuum tests were done to test for leaks. Measurements with pressure and temperature dependencies were done to characterize the nozzle. Finally, TOF characterizations were made, including dark count measurements (without laser) and varying the MCP back voltage, followed by variation of extractor and repeller voltages, solenoid current, position of the magnet-manipulator and MCP front voltage.

4.1   Vacuum tests

Every flange component was tested for leaks with a He leak tester. Also, a suitable way to check for leaks is to pour some ethanol on the flanges. If it gets sucked inside the chamber, there is a leak - if not, the ethanol vaporizes after a short time without residuals. The prevac pumps achieved a pressure in the lower 1×10^{-3} mbar regime in both chambers. Before connecting the chambers, a pressure in the lower 1×10^{-5} mbar in the source chamber (without nozzle implemented) and the lower 1×10^{-8} mbar in the main

chamber was reached without bakeout. With all components built in and the chambers connected, a bakeout was performed for about 30 hours. To prevent the system from over-heating, the currents of the heating bands were slowly increased within several hours to a maimum temperature of 73.7°C at the solenoid. Figure 4.1 shows the QMS signal with the same atomic masses as in figure 3.18 before and after the bakeout. Clearly, the signal decreased and a pressure value in the lower 1×10^{-9} mbar regime was obtained. After a startup phase, all three turbo pumps operated at minimum load. Thus, major leaks can be excluded.

4.2   First He tests

The first measurement for a molecular beam was done with He only, therefore after installing the nozzle. All turbomolecular pumps were turned on and the He pressure was varied with and without heating of the nozzle.

In figure 4.2 the pressure of the SC as a function of the He pressure (yellow line) and the estimated base pressure with equation 3.1 (red dashed line) are shown. Also, the effective pressure of the gauge was calculated for He according to 3.2 and described in section 3.6 (blue dashed line). The He pressure was varied up to 4 bar, which was near the limit for the turbo pumps according to the manual. An expected linear behavior could be measured. The calculated mean deviation between the calculation and the measurement was 4.0713×10^{-5} mbar.
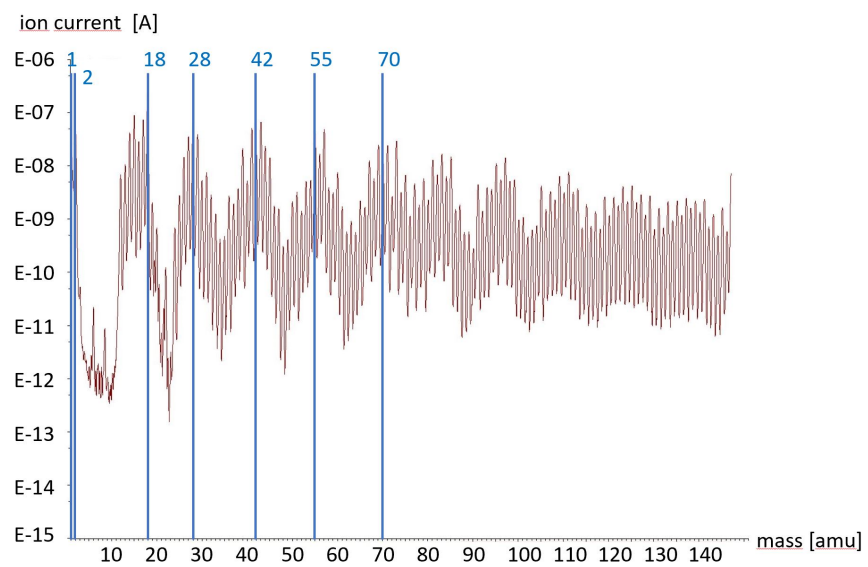
(a) before bakeout
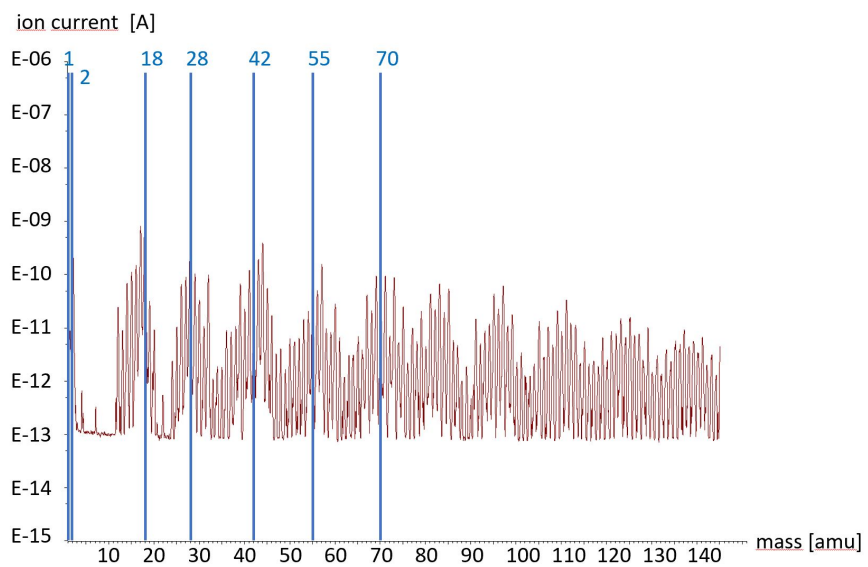
(b) after bakeout

Figure 4.1: QMS signal before and after bakeout
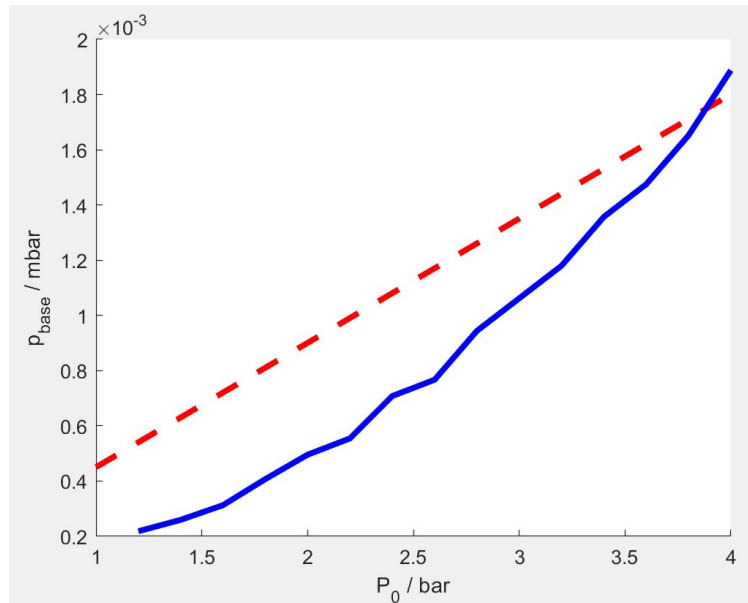
Figure 4.2: Dependency of pressures in source chamber on He gas pressure at $T_0 = 300$ K in comparison to the calculated value (red dashed line) and the measurement, considering the gauge conversion factor (equation 3.2) for the effective pressure for He (blue line).

Figure 4.3 shows the pressure of the SC as a function of the nozzle heating. A constant He pressure of 1.2 bar was applied and only the nozzle top was heated up to 80°C. The temperature dependency, according to equation 3.1 is proportional to $\frac{1}{\sqrt{T_0}}$, however, at 20° to 60°C the graph looks quite linear. This is due to the fact that the unit [K] was used and the slope doesn't change that much anymore.
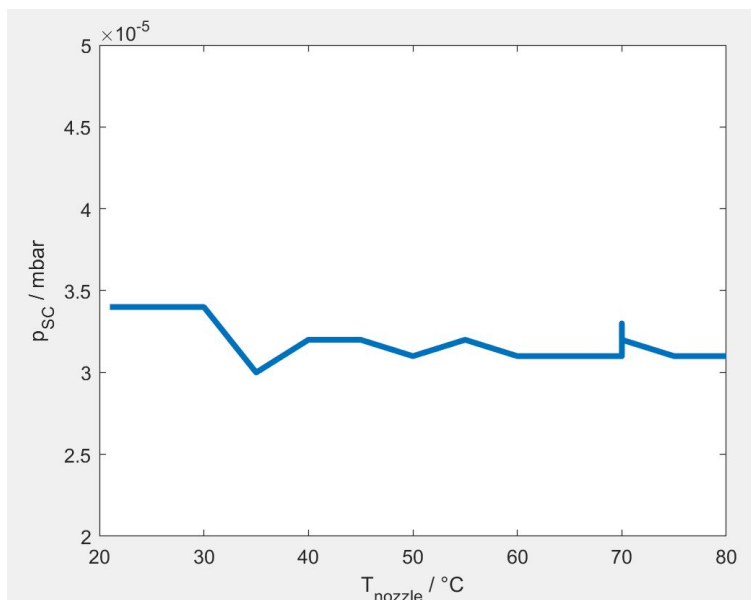
Figure 4.3: Dependency of source chamber pressure on nozzle temperature with 1.2 bar He pressure.

Within the first tests, the He flow was lower than expected and the nozzle was examined with a light microscope to exclude a clogging. Fortunately, the figures 4.4 show no clogging. These pictures should be taken as model if the nozzle is examined again.
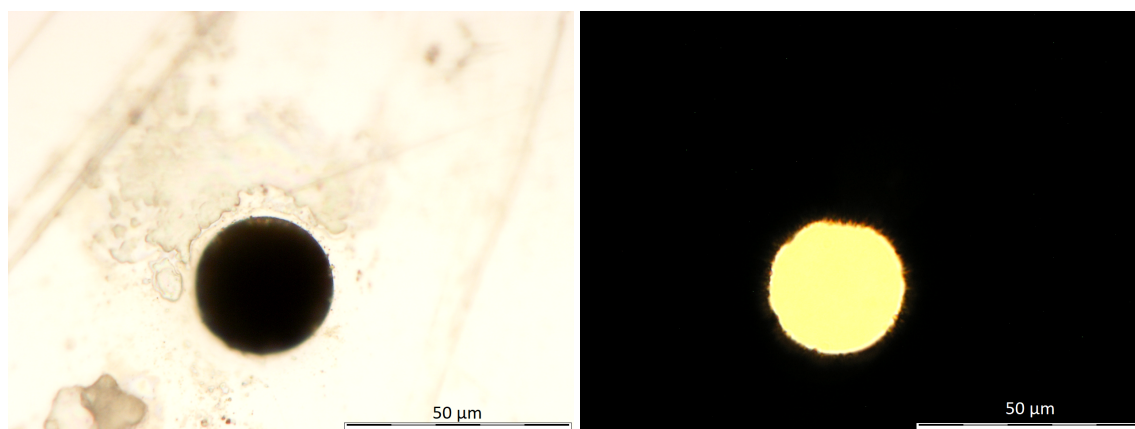
(a) reflection measurement

(b) transmission measurement

Figure 4.4: Examination of the nozzle with a light microscope.

4.2.1 Nozzle alignment

The nozzle was moved to optimize the alignment by maximizing the QMS signal 4 which corresponds to He. This was done at 9.8×10^{-8} mbar in the main chamber and 2.1×10^{-5} mbar in the source chamber and 1 bar He was applied. The optimal position of the manipulator was found at:

x-position: 3.31 mm

y-position: 2.69 mm

4.3 First heating tests

To ensure a temperature gradient, only the nozzle top was heated at first. According to figure 3.6 the nozzle top is the far most left heating band and nearest to the nozzle. This measurement should cover the case of nozzle temperatures up to 60°C. The turbo pumps were turned on and a He pressure of 1.2 bar was applied. At time 0 the controller was set to 60°C (nozzle top).

After 15 minutes, the nozzle top was at the desired temperature and was stable until the end of the measurement at 3 hours, as seen in figure 4.5. At these temperatures, a heating of the other parts of the nozzle is not recommendable, because the nozzle top must always be the hottest part. However, going to higher temperatures, an optional heating will be possible with the transistor controller circuit from figure 3.8.

4.4 TOF Characterization

To optimize the electron yield, the MCP was characterized by varying different parameters. The following measurements were all done with the same 800 nm laser and a 500 mm
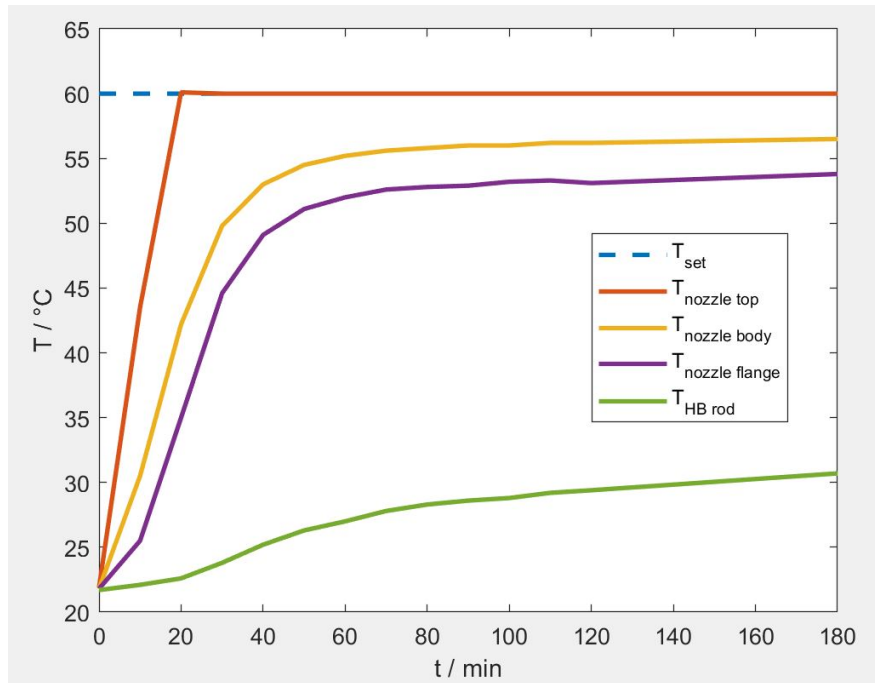
Figure 4.5: Dependency of the temperatures on the different parts of the heated nozzle body

lens for focusing inside the main chamber. The anode was always set to the voltage at the MCP back + 500 V according the the manual of the MCP.

4.4.1 Variation of the MCP back voltage

To investigate dark counts only, the following measurement was done without laser. If the MCP back voltage is increased, the electrons are accelerated more and the signal will be higher. The settings from table 4.1 were used and the MCP back voltage was varied to investigate dark counts, as seen in figure 4.6 (left without and right with Acetone). An expected increase of the signal could be measured. Comparing 4.6(a) with 4.6(b), there seems to be no effect at all if acetone is in the chamber or not.

Table 4.1: Settings for dark count measurements with and without acetone

anode	MCP back + 500 V
MCP back	varied
MCP front	GND
repeller	GND
extractor	GND
wavelength	800 nm
power	0 mW (laser off)
lens	500 mm
MC Pressure (left figure)	9×10^{-9} mbar
MC pressure with Acetone (right figure)	2×10^{-6} mbar
integration time	5 s
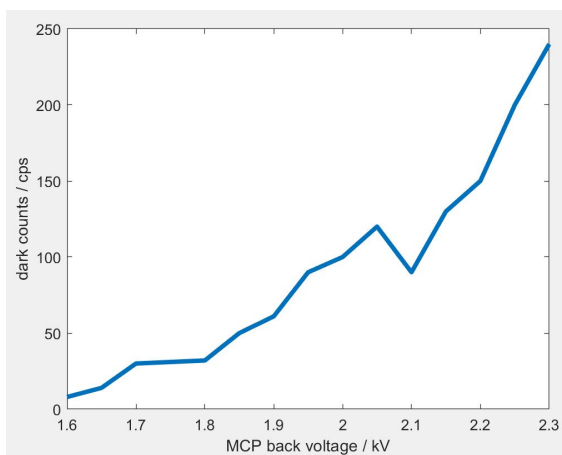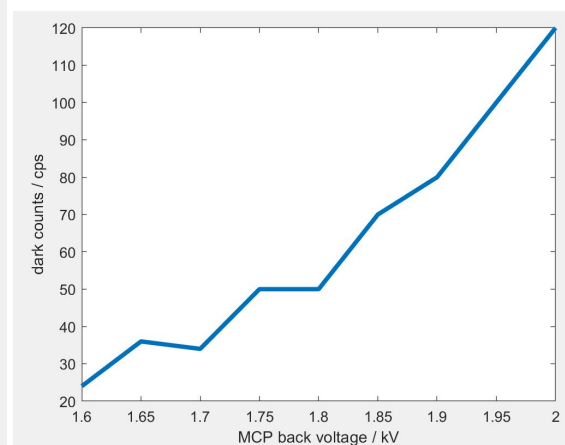
(a) without Acetone   (b) with Acetone

Figure 4.6: Dark count measurement as a function of MCP back voltage without (a) and with (b) acetone in the main chamber.

4.4.2 Variation of the extractor voltage

Next, the extractor voltage was varied with the settings from table 4.2 and the repeller voltage was set to 2 kV to measure ions. The measurement is shown in figure 4.7. First, an increase of the signal could be measured up to an extractor voltage of about 1.6 kV, followed by a rapid decrease. If an extractor voltage of 2 kV is applied, there is an inhomogeneous field between repeller and extractor because of the geometry. Here, the lens effect of the extractor decreases. The reason why there still is a signal might be because the field still accelerates some ions. Also, ions can have a kinetic energy large enough to leave the ionization area and are accelerated from the extractor to the TOF which is grounded.

Table 4.2: Settings for different extractor voltages

anode	MCP back + 500 V
MCP back	1.9 kV
MCP front	GND
repeller	2 kV
extractor	varied
wavelength	800 nm
power	110 mW
lens	500 mm
MC pressure with acetone	2×10^{-6} mbar
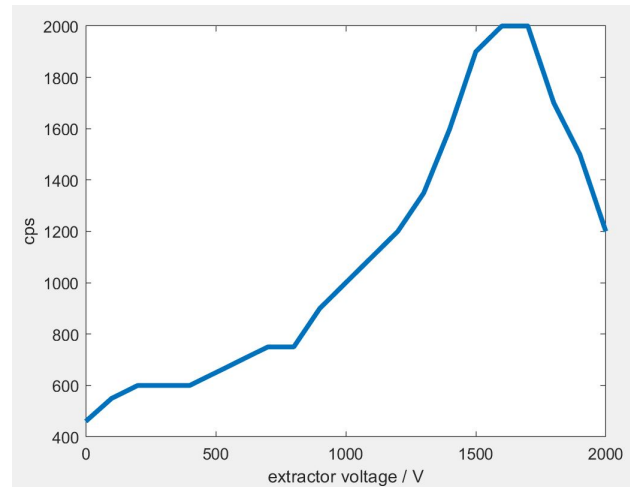
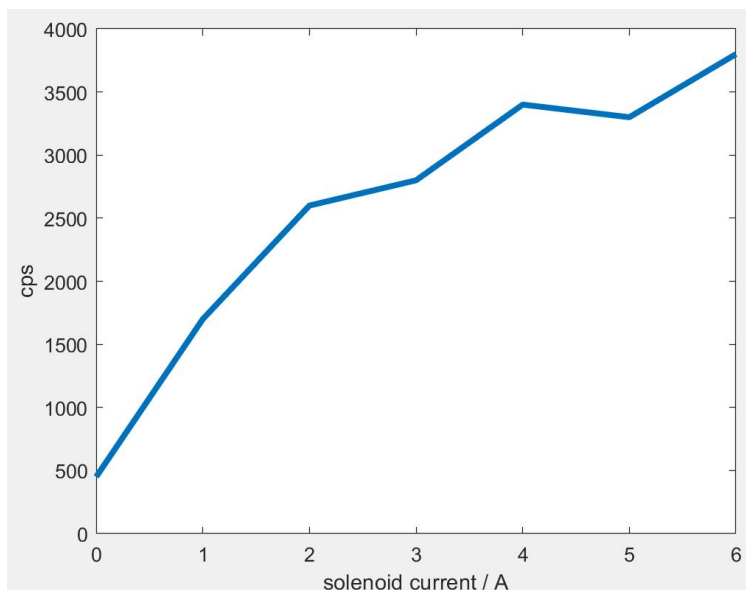**Figure 4.7:** Total counts per second as a function of extractor voltage

4.4.3 Variation of the repeller voltage

To investigate the repeller voltage dependency, the voltage was switched back to negative for investigating electrons and a solenoid current of 3 A was applied for the magnetic bottle effect. By applying a negative repeller voltage, the electrons are driven away from the repeller towards the MCP. Therefore, an increase of the signal is expected. If the repeller voltage is positive, the electrons tend to move in the direction of the repeller rather than towards the MCP. Table 4.3 shows the settings for the measurement and the result is shown in figure 4.8. In theory, the graph should look like a step function from 1 to 0 at V=0. Starting at -10 V there seems to be a jump which can be explained with fluctuations. Actually, there should be a constant plateau. Between -4 V to -1 V there is a slow decrease. This could be due to electrons that start in direction of the repeller and are first slowed down before accelerated to the MCP. A strong decrease starting at -1 V could be measured as expected. There is some signal left at 2 V, because the electrons with a high kinetic energy in direction towards the MCP can still be detected.

Table 4.3: Settings for varying repeller voltage

anode	MCP back + 500 V
MCP back	1.9 kV
MCP front	GND
repeller	varied
extractor	GND
repeller z-position	60 mm
wavelength	800 nm
power	88 mW
lens	500 mm
MC pressure with Acetone	2×10^{-6} mbar
integration time	5 s
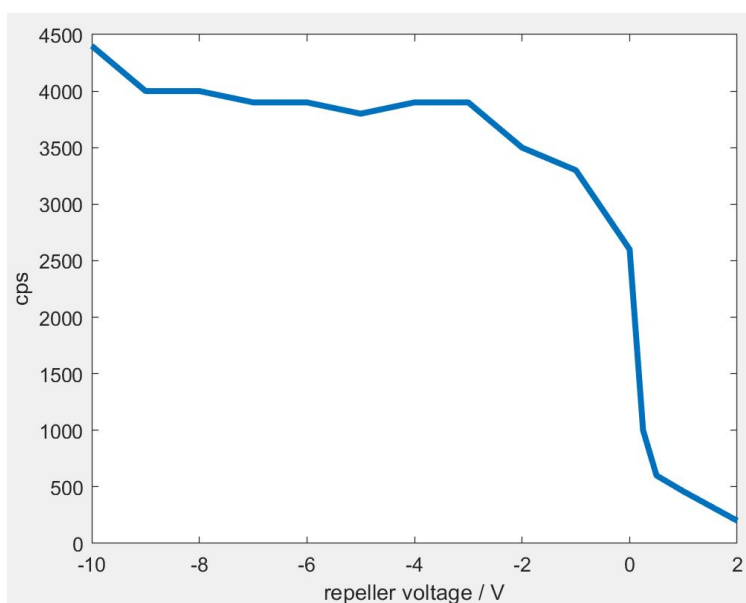
Figure 4.8: Total counts per second as a function of repeller voltage

4.4.4 Variation of the solenoid current

The variation of the solenoid current should affect the electron signal. A higher current leads to closer magnetic field lines and the electrons are led to the MCP leading to a better detection efficiency. This was measured with acetone and the settings from table 4.4 and the signal is shown in figure 4.9. An expected increase of the signal can be seen from 0 A to 6 A, like in [34] on page 31.

Table 4.4: Settings for varying solenoid current

anode	MCP back + 500 V
MCP back	1.9 kV
MCP front	GND
repeller	-3 V
extractor	GND
solenoid current	varied
repeller z-position	60 mm
wavelength	800 nm
power	88 mW
lens	500 mm
MC pressure with Acetone	2×10^{-6} mbar
integration time	5 s

Figure 4.9: Total counts per second as a function of solenoid current

4.4.5 Variation of the repeller position

The repeller position is significant for optimizing the signal. Figure 4.10 shows the directions of the laser and the molecular beam and the used coordinate system. One turn on the repeller manipulator is equal to 1 mm. From the biggest distance between magnet and repeller, the z-value was taken. The magnet almost touches the plate at the absolute value of the repeller at z = 97 mm, which will be the new z-origin (z = 0). The laser focus is situated about 3 mm above the 2 mm thick repeller plate. An increase in the repeller-magnet-distance leads to a negative z-value.

The x,y and z positions of the magnet on the repeller were varied with the settings from table 4.5 and the measurements with electrons are shown in figure 4.11. An increase in the distance leads to following effects:

- the x- and y-dependencies seem to be unchanged

- the width of the y-positions increases
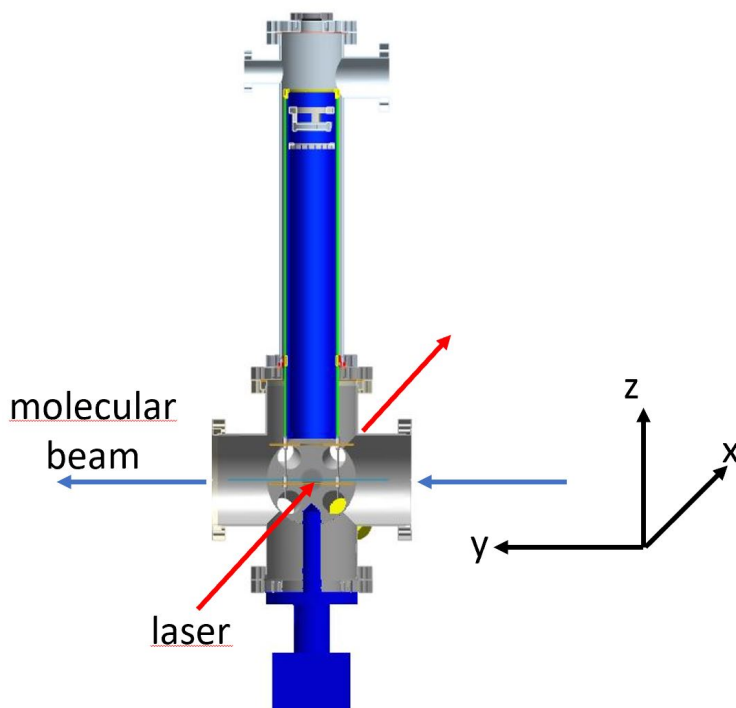
Figure 4.10: Coordinates of the repeller

- the total counts increase

In comparison with [34] on page 42, the full width at half maximum (FWHM) is much broader. This might be due to a new setup with better magnets. With this setup, more signal can be obtained, however, also more heat will be created.

Table 4.5: Settings for varying x, y and z positions of the magnet attached to the repeller

anode	MCP back + 500 V
MCP back	1.9 kV
MCP front	GND
repeller	-3 V
extractor	GND
solenoid current	6 A
repeller z-position	varied
wavelength	800 nm
power	100 mW
lens	500 mm
MC pressure with Acetone	2×10^{-6} mbar
integration time	1 s
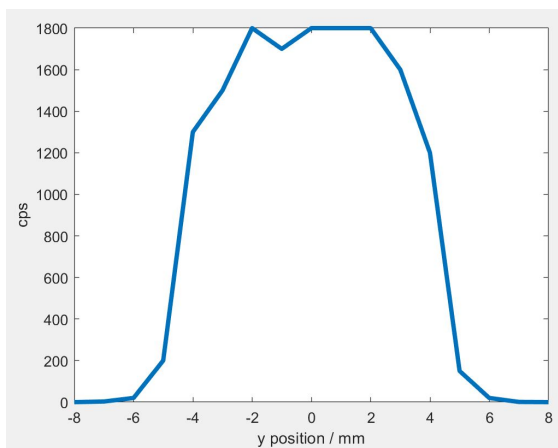
(a) z = -12 mm, y scan mm
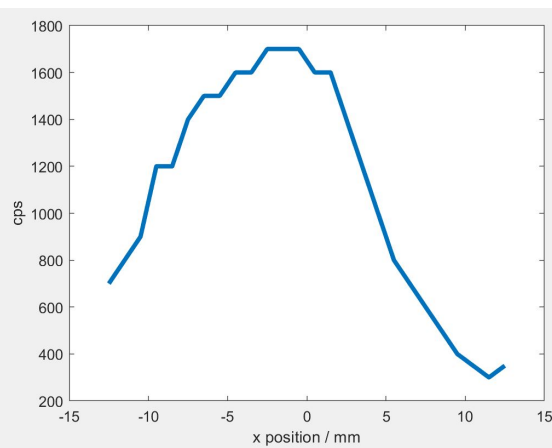
(b) z = -12 mm, x scan mm
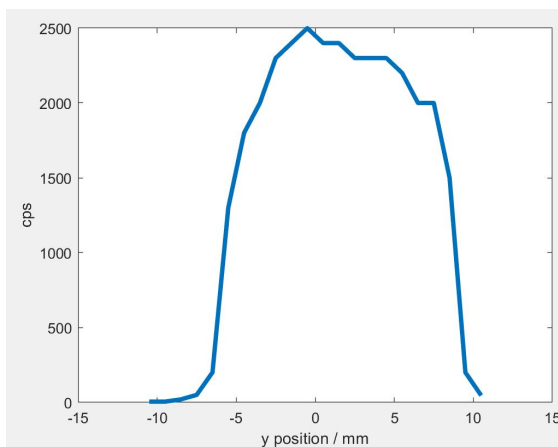
(c) z = -24 mm, y scan mm
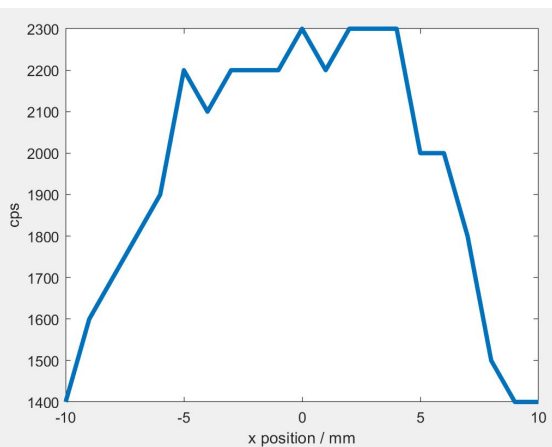
(d) z = -24 mm, x scan mm
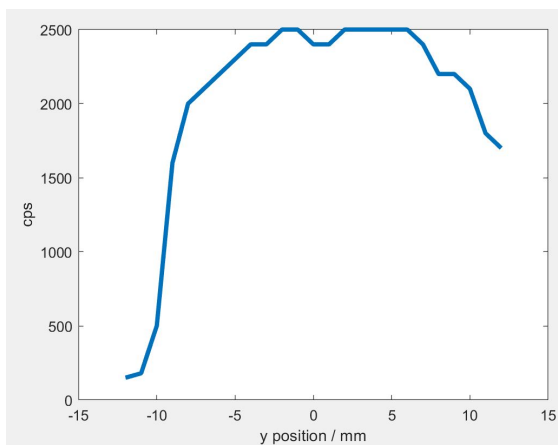
(e) z = -36 mm, y scan mm
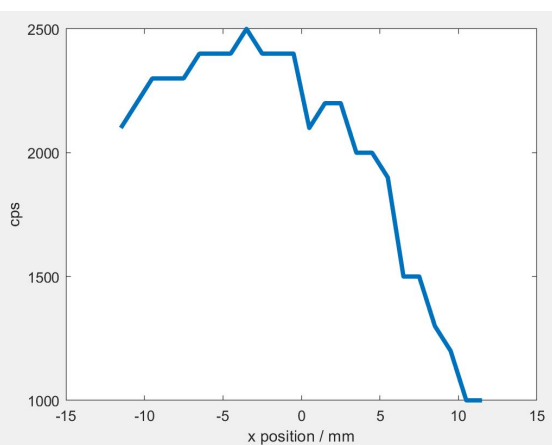
(f) z = -36 mm, x scan mm

Figure 4.11: x,y and z position variations of the repeller

4.4.6 Variation of the MCP front voltage

Finally, the MCP front voltage was varied with the settings of table 4.6. If the potential between MCP front and MCP back is too small, the accelerated electrons have less energy and therefore less signal is detected. However, the measurement only showed a small effect on the total counts. A negative MCP front voltage showed a smaller signal, but only about 25% less - even though no signal at all would be expected if the MCP front voltage is high enough. This could be explained with the high resistivity of the MCP which could lead to an inhomogeneous potential on the MCP surface.

Table 4.6: Settings for varying MCP front voltage

anode	MCP back + 500 V
MCP back	1.9 kV
MCP front	varied
repeller	-3 V
extractor	GND
solenoid current	6 A
repeller z-position	60 mm
wavelength	800 nm
power	88 mW
lens	500 mm
MC pressure with Acetone	2×10^{-6} mbar
integration time	1 s

List of plots

List of tables

References

[1] S. Chu, W. Li, Y. Yan, T. Hamann, I. Shih, D. Wang and Z. Mi, *Roadmap on solar water splitting: current status and future prospects*, Nano Futures, 1, 022001 (2017)

[2] A. Kudo, Y. Miseki, *Heterogeneous photocatalyst materials for water splitting*, Chemical Society Reviews, 38, 253-278 (2008)

[3] A. L. Sobolewski, W. Domcke, *Computational Studies of the Photophysics of Hydrogen-Bonded Molecular Systems*, J. Phys. Chem. A, 111, 11725-11735 (2008)

[4] A. L. Sobolewski and W. Domcke, *Photoinduced water splitting with oxotitanium porphyrin: a computational study*, Phys. Chem. Chem. Phys., 14, 12807-12817 (2012)

[5] X. Liu, A. L. Sobolewski, R. Borrelli, W. Domcke, *Computational investigation of the photoinducedhomolytic dissociation of water in the pyridine-water complex*, Phys. Chem. Chem. Phys., 15, 5957 (2013)

[6] X. Liu, A. L. Sobolewski and W. Domcke, *Photoinduced oxidation of water in the pyridine-water-complex: Comparison of the singlet and triplet photochemistries*, Phys. Chem. Chem. Phys., 118, 7788-7795 (2014)

[7] O. Morawski, K. Izdebska, E. Karpiuk, J. Nowacki, A. Suchocki, A. L. Sobolewski, *Photoinduced water splitting with oxotitanium tetraphenylporphyrin*, Phys. Chem. Chem. Phys., 16, 15256-15262 (2014)

[8] X. Liu, T. N. V. Karsili, A. L. Sobolewski and W. Domcke, *Photocatalytic Water Splitting with the Acridine Chromophore: A Computational Study*, J. Phys. Chem. B, 119, 10664-10672 (2015)

[9] T. N. V. Karsili, D. Tuna, J. Ehrmaier and W. Domcke, *Photoinduced water splitting via benzoquinone and semiquinone sensitisation*, Phys. Chem. Chem. Phys., 17, 32183-32193 (2015)

[10] O. Morawski, K. Izdebska, E. Karpiuk, A. Suchocki, Y. Zhydachevskyy and A. L. Sobolewski, *Titanyl Phthalocyanine as a Water Photooxidation Agent*, J. Phys. Chem. C, 119, 14085-32193 (2015)

[11] X. Liu, T. N. V. Karsili, A. L. Sobolewski and W. Domcke, *Photocatalytic water splitting with acridine dyes: Guidelines from computational chemistry*, Chemical Physics, 464, 78-85, (2016)

[12] J. Ehrenmaier, T. N. Karsili, A. L. Sobolewski, W. Domcke, *Mechansim of Photocatalytic Water Splitting with Graphic Carbon Nitride: Photochemistry of the Heptazine-Water Complex*, J. Phys. Chem. A, 121, 4754-4764 (2017)

[13] N. Esteves-Lopez, S. Coussan, C. Dedonder-Lardeux, C. Jouvet, *Photoinduced water splitting in pyridine water clusters*, Phys. Chem. Chem. Phys., 18, 25637-25644 (2016)

[14] J. R. Reimers and Z.-L. Cai, *Hydrogen bonding and reactivity of water to azines in their S1 (n,*) electronic excited states in the gas phase and in solution*, Phys. Chem. Chem. Phys., 14, 8791-8802 (2012)

[15] I. V. Hertel and W. Radloff, *Ultrafast dynamics in isolated molecules and molecular clusters*, Reports Prog. Phys., 69, 1897-2003 (2006)

[16] H. Lippert, V. Stert, L. Hesse, C. P. Schulz, I. V. Hertel and W. Radloff, *Analysis of Hydrogen Atom Transfer in Photoexcited Indole(NH3)n Clusters by Femtosecond Time-Resolved Photoelectron Spectroscopy*, J. Phys. Chem. A, 107, 8239-8250 (2003)

[17] A. L. Sobolewski, W. Domcke, C. Dedonder-Lardeux, and C. Jouvet, *Excited-state hydrogen detachment and hydrogen transfer driven by repulsive 1* states: A new paradigm for nonradiative decay in aromatic biomolecules*, Phys. Chem. Chem. Phys., 4, 10931100 (2002)

[18] Z. Lan, W. Domcke, V. Vallet, A. L. Sobolewski, and S. Mahapatra *Time-dependent quantum wavepacket description of the * photochemistry of phenol*, The Journal of Chemical Physics, 122, 224315 (2005)

[19] H. Lippert, H. Ritze, I. V. Hertel, and W. Radloff, *Femtosecond time-resolved hydrogen-atom elimination from photoexcited pyrrole molecules*, ChemPhysChem, 5, 14231427 (2004)

[20] G. M. Roberts and V. G. Stavros, *The role of * states in the photochemistry of heteroaromatic biomolecules and their subunits: insights from gas-phase femtosecond spectroscopy*, Chem.Sci., 5, 1698 (2014)

[21] P. Chakraborty, T. Karsili, B. Marchetti, and S. Matsika, *Mechanistic insights into photoinduced damage of DNA and RNA nucleobases in the gas phase and in bulk solution*, Faraday Discussions, 207, 329350, (2018)

[22] P. Maierhofer, M. Bainschab, B. Thaler, P. Heim, W. E. Ernst and M. Koch, *Disentangling Multichannel Photodissociation Dynamics in Acetone by Time-Resolved Photoelectron-Photoion Coincidence Spectroscopy*, J. Phys. Chem. A 120, 6418-6423 (2016)

[23] M. Koch, P. Heim, B. Thaler, M. Kitzler and W. E. Ernst, *Direct observation of a photochemical observation energy: a case study of acetone photodissociation*, Journal of Physics B: Atomic, Molecular and Optical Physics 50, 125102 (2017)

[24] M. Koch, B. Thaler, P. Heim and W. E. Ernst, *The role of rydbergvalence coupling in the ultrafast relaxation dynamics of acetone*, J. Phys. Chem. A, 121, 6398-6404 (2017)

[25] Légaré, F. and Lee, Kevin F. and Litvinyuk, I. V. and Dooley, P. W. and Bandrauk, A. D. and Villeneuve, D. M. and Corkum, P. B., *Imaging the time-dependent structure of a molecule as it undergoes dynamics*, Phys. Rev. A, 72, 052717 (2005)

[26] K. Schwinghammer, B. Tuffy, M. B. Mesch, E. Wirnhier, C. Martineau, F. Taulelle, W. Schnick, J. Senker and B. V. Lotsch, *Trianzine-base carbon nitrides for visible-light-driven hydrogen evolution*, Angewandte Chemie International Edition, 52, 2435-2439 (2013)

[27] R. Trebino, K. W. DeLong, D. N. Fottinghoff, J. N. Sweetser, M. A. Krumbgel, B. a. Richman, D. J. Kane, *Measuring ultrashort laser pulses in the time-frequency domain using frequency-resolved optical gating*, Rev. Sci. Instrum., 68, 3277-3295 (1997)

[28] H. Lippert, *Ultrakurzzeitspektroskopie von isolierten und mikrosolvatisierten Biochromophoren*, Ph.D. thesis, Freie Universitt Berlin, (2005)

[29] Pfeiffer PKR 261 Compact FullRange Gauge manual, www.fe.infn.it, (2019/06/24)

[30] Electrolysis, https://www.energy.gov(2019/06/24)

[31] Fuel Cell, https://en.wikipedia.org, (2019/06/24)

[32] Wiley McLaren Setup, www.ipc.kit.edu, (2019/06/24)

[33] W: C: Wiley and I. H. McLaren, *TimeofFlight Mass Spectrometer with Improved Resolution*, Review of Scientific Instruments, 26, 1150-1157 (1955)

[34] M. Bainschab, *Multiphoton Ionization Channels in Molecules Investigated by Photoelectron-Photoion-Coincidence Spectroscopy*, Master's thesis, TU Graz, (2016)

[35] P. Maierhofer, *Femtosecond Photodissociation Dynamics in Molecules studied by Time-Resolved Photoelectron-Photoion-Coincidence Spectroscopy*, Master's thesis, TU Graz, (2016)

[36] S. Ranftl, *Ultrafast Photoinduced Ejection Dynamics of Indium Atoms inside Superfluid Helium Nanodroplets*, Master's thesis, TU Graz (2017)

[37] M. Koch, *Magnetic Resonance Spectroscopy of Single Alkali-Metal Atoms Isolated in Superfluid Helium Nanodroplets*, Dissertation, TU Graz, (2009)

[38] Properties of chromophores used, https://pubchem.ncbi.nlm.nih.gov, (2019/06/24)

[39] Properties of chromophores used, https://www.chemicalbook.com, (2019/06/24)

[40] Schematic of a chevron MCP, http://inspirehep.net, (2019/06/24)

[41] J. Ullrich, R. Moshammer, A. Dorn, R. Drner, L. Schmidt and H. Schmidt-Bcking, *Recoil-Ion and Electron Momentum Spectroscopy: Reaction-Microscopes*, Reports on Progress in Physics, 66, 1463-1545, (2003)

Danksagung

Zum Abschluss möchte ich noch allen danken, die mich im Studium in den letzten Jahren und in dieser Arbeit im vergangenen Jahr unterstützt haben.

Vielen Dank an Assoc.Prof. Dipl.-Ing. Dr.techn. Markus Koch für die großartige Möglichkeit, an einem interessanten Projekt wie diesem teilnehmen zu können. Danke auch dafür, selbstständig arbeiten zu können und für das Vertrauen, als Student mit komplizierten technischen Geräten hantieren zu dürfen. Ich wünsche Dir noch viele Förderungen und dass dieser Bereich der Forschung weltweit Anklang findet.

Danke Pascal Heim, der mich die ganze Zeit sehr gut betreut hat. Du hast mir immer mehr zugetraut als ich mir selber und im dadurch habe ich sehr viel Erfahrung und Selbstbewusstsein gesammelt. Auch für Dich hoffe ich, dass deine Doktorarbeit positiv angenommen wird und Du in diesem Bereich Erfolg haben wirst.

Danke Bernhard für die Beantwortung sämtlicher Fragen, die ich whrend meiner Zeit hatte und auch für den Einblick in das Femtolab I, in dem ich zu Beginn einige Zeit verbracht habe und sogar ein paar Messungen eigenständig durchführen habe dürfen.

Danke Leo für die Unterstützung und den Einblick in die transiente Absorp-

tion. Außerdem für die fast wöchentlichen Abstimmungen ber Themen wie "Beatles, oder Beach Boys" (Die Antwort ist Beatles).

Vielen Dank auch an Univ.-Prof. Dipl.-Phys. Dr.rer.nat. Wolfgang Ernst, dass ich nach meiner Bachelorarbeit bei Ihnen auch die Möglichkeit hatte, praktische Erfahrung am Institut für Experimentalphysik zu sammeln.

Auch den MitarbeiterInnen des Sekretariats und des Dekanats an der TU Graz gilt ein besonderer Dank für die schnelle Abwicklung sämtlicher Fragen, die sich bezüglich Studium und auch Anstellung, sowie Abschluss des Studiums ergeben haben.

Ein besonderer Dank gilt auch meinen Eltern, die mich mit sehr viel Geduld und Finanzen unterstützt haben, was sich schlussendlich auch gelohnt hat! Danke Mama für all die Mama-Sachen. Es behauptet zwar jeder, dass seine Mama die beste ist, aber das sind alles nur Lügen! Danke Papa für die großartige Unterstützung in vielen Bereichen und dass Du mich im Würfelpoker immer gewinnen lässt. Natrlich danke ich auch meiner Tante Eva und meiner Gromutter Nana, sowie meinem Bruder Peter, meiner Schwägerin Steff und der mittlerweile gar nicht mehr so kleinen Maya für ein sehr angenehmes familiäres Verhältnis, nicht nur während des Studiums.

Mein leider bereits verstorbener Grovater Toni soll hier extra erwähnt werden. Danke für die oft sehr langen Diskussionen über nicht nur physikalische Themen und Deine Weitsicht auf mehreren Ebenen. Ich hätte mit Dir gerne über die moderne Physik gesprochen, da ich jetzt mehr verstehe und wir uns mittlerweile vielleicht sogar in der selben technischen Sprache unterhalten hätten können. Danke, dass Du nicht nur ein sehr lieber Grovater, sondern auch ein guter Freund warst.

Danke Janina, dass wir uns gegenseitig unterstützen und es in den letzten Jahren nie zu einer Streiterei gekommen ist! Vielleicht sollten wir daher heiraten (, wobei dies nicht als Antrag gilt).

Vielen Dank auch für die ausgleichsreichen Stunden an meine Mitmusiker, sowie befreundete Bands und auch für die gute Musik, die ich teilweise beim Lernen gehört habe! Danke den Mitstudenten, ohne die ich vermutlich nicht dort wäre, wo ich jetzt bin. Abschließend danke ich all meinen restlichen Freunden. Und Matzi.